



저작자표시-비영리-변경금지 2.0 대한민국

이용자는 아래의 조건을 따르는 경우에 한하여 자유롭게

- 이 저작물을 복제, 배포, 전송, 전시, 공연 및 방송할 수 있습니다.

다음과 같은 조건을 따라야 합니다:



저작자표시. 귀하는 원저작자를 표시하여야 합니다.



비영리. 귀하는 이 저작물을 영리 목적으로 이용할 수 없습니다.



변경금지. 귀하는 이 저작물을 개작, 변형 또는 가공할 수 없습니다.

- 귀하는, 이 저작물의 재이용이나 배포의 경우, 이 저작물에 적용된 이용허락조건을 명확하게 나타내어야 합니다.
- 저작권자로부터 별도의 허가를 받으면 이러한 조건들은 적용되지 않습니다.

저작권법에 따른 이용자의 권리는 위의 내용에 의하여 영향을 받지 않습니다.

이것은 [이용허락규약\(Legal Code\)](#)을 이해하기 쉽게 요약한 것입니다.

[Disclaimer](#)

공학박사 학위논문

레이저-구리 나노 입자 상호작용
공정을 활용하여 산화 억제된 유연
하고 투명한 구리 전자소자 제작

Oxidation-suppressed Flexible and
Transparent Cu Electronics by
Laser-Cu Nanoparticles
Interaction

2019 년 2 월

서울대학교 대학원

기계항공공학부

조 현 민

Abstract

Copper nanomaterials suffer from severe oxidation problem despite the huge cost effectiveness. The effect of two different processes for conventional tube furnace heating and selective laser sintering on copper nanoparticle paste is compared in the aspects of chemical, electrical and surface morphology. The thermal behavior of the copper thin films by furnace and laser is compared by SEM, XRD, FT-IR and XPS analysis. The selective laser sintering process ensures low annealing temperature, fast processing speed with remarkable oxidation suppression even in air environment while conventional tube furnace heating experiences moderate oxidation even in Ar environment. Moreover, the laser-sintered copper nanoparticle thin film shows good electrical property and reduced oxidation than conventional thermal heating process. Consequently, the proposed selective laser sintering process can be compatible with plastic substrate for copper based flexible electronics applications.

We developed a simple and cost-effective Cu patterning method on a flexible PET film by combining a solution processable Cu nanoparticle patterning and a low temperature post-processing using acetic acid treatment, laser sintering process and acid-assisted laser sintering process. Acid-assisted laser sintering processed Cu electrode showed superior characteristics in electrical, mechanical and chemical stability over other post-

processing methods. Finally, the Cu electrode was applied to the flexible electronics applications such as flexible and transparent heaters and touch screen panels.

Active control of transparency/color is the key to many functional optoelectric devices. Applying electric field to electro-chromic or liquid crystal material is the typical approach for optical property control. In contrast to conventional electro-chromic method, we developed a new concept smart glass using totally new driving mechanism (mechanical stimulus and thermal energy) to control the optical properties of the salt hydrate. This developed mechano-thermo-chromic smart glass device with the integrated transparent micro heater uses the sodium acetate solution which shows a unique dramatic optical property change under mechanical impact (mechano-chromic) and heat (thermo-chromic). The developed mechano-thermo-chromic devices may provide useful approach in the future smart window applications that operates by an external environment condition.

Keyword : Oxidation-suppressed, Copper nanoparticles, Selective Laser Sintering, Acid-assisted Laser Sintering Process, Flexible and transparent electrode array

Student Number : 2014-21833

Table of Contents

Chapter 1. Introduction.....	1
1.1 Study Background	1
1.2 Purpose of Research	5
 Chapter 2. Material synthesis and process setting	10
2.1 Copper nanoparticles synthesis	10
2.2 Selective Laser sintering.....	11
2.3 Cu nanoparticle mold transfer method.....	12
2.4 ALSP process.....	12
2.5 Smart glass application	13
2.6 Material Characterization.....	14
 Chapter 3. Experimental result : selective laser sintering of	
 copper nanoparticles	17
3.1 Copper nanoparticles synthesis and Laser optical setting...17	
3.2 Thermal behavior of copper nanoparticles	19
3.3 Optimum condition of SLS process	21
3.4 Comparison of thermal annealing and SLS process	24
3.5 Chemical stability of Cu nanoparticles processed by thermal annealing and SLS process.....	27
3.6 Flexible and transparent conductor with SLS process	32

Chapter 4. Experimental result : acid–assisted laser sintering process (ALSP) of copper nanoparticles	43
4.1 Mold transfer process.....	43
4.2 Post process (AAT, LSP, ALSP)	45
4.3 Optimum condition of ALSP.....	47
4.4 Chemical electrical and mechanical stability	50
4.5 XPS analysis with process (AAT, LSP, ALSP)	53
4.6 Stable Joule heater demonstration.....	56
 Chapter 5. Experimental result : Mechano–thermo–chromic device with phase change and ALSP process....	64
5.1 Operating mechanism.....	64
5.2 Fabrication of MTC device	68
5.3 Design of MTC device.....	71
5.4 Phase transition behavior of MTC device.....	76
5.5 Application of MTC device for smart glass	81
 Chapter 6. Summary and future work	90
 References.....	93
 Abstract in Korean	99

Table of Contents

Figure 1 Surface morphology and Schematics of the laser sintering system

Figure 2 TG–DTA measurement for the copper nanoparticle paste

Figure 3 A parametric study on laser sintering for various laser power and scanning speed

Figure 4 Comparison of Cu NP thin film surface morphology by furnace thermal annealing in Ar environment and by laser sintering in air

Figure 5 Comparative study on the XPS analysis for the as prepared, furnace thermal annealing and laser sintered Cu NP thin films

Figure 6 Flexible Cu grid transparent conductor on the PEN film by selective laser sintering of Cu NPs

Figure 7 The thickness of the laser–sintered and non–sintered copper thin film on the glass substrate is presented

Figure 8 The absorption spectrum of as–prepared Cu thin film on glass substrate

Figure 9 The compared sheet resistance of the copper samples

Figure 10 A simple parametric study on the laser sintering for laser power and scan speed

Figure 11 The topological AFM images of the laser–sintered Cu conductive line on PEN film

Figure 12 Designed simple Cu pattern sample and Electrical resistivity of before/after laser sintering process on the sample

Figure 13 Tape test results for the selective laser sintered Cu thin film on the PEN film

Figure 14 Schematic illustration of the Cu NP patterning and transfer to the flexible substrate

Figure 15 A schematic illustration of the post-processing methods for acetic acid treatment (AAT), laser sintering process (LSP) and acid-assisted laser sintering process (ALSP)

Figure 16 Parametric study on the laser sintering process for laser power and scanning speed to find optimum condition of the electrical conductivity and surface morphology

Figure 17 The chemical, electrical and mechanical stability test of Cu electrodes for various post treatment methods

Figure 18 XPS characterization is verified on the Cu electrode after various post-treatment methods for AAT, LSP and ALSP

Figure 19 Transparent and flexible Cu Joule heater demonstration

Figure 20 Applications in flexible electronics

Figure 21 The sheet resistance changes of as-prepared Cu NP thin film with acetic acid immersion time

Figure 22 Cyclic bending test results for LSP and ASLP treated samples

Figure 23 The XPS analysis for as-prepared Cu NP. The Cu NPs are slightly oxidized, which arise from the nanoparticle synthesis procedure

Figure 24 The XRD characterization of as-prepared, AAT, ASP and ALSP treated Cu NPs before and after high humidity-temperature test

Figure 25 Solubility graph at different temperature for sodium acetate anhydrous (CH_3COONa , red line) and sodium acetate trihydrate ($\text{CH}_3\text{COONa} \cdot 3\text{H}_2\text{O}$, black line) where the solid lines indicate saturated state

Figure 26 The fabrication process of MTC device which consisted of a chamber for sodium acetate solution and the transparent micro heater processed prepared by acid-assisted laser sintering of Cu nanoparticle paste

Figure 27 The transient temperature measurement and corresponding IR camera images for the electro-thermal performance and temperature distribution

Figure 28 Real time measurement and calculation of temperature and transmission change during the phase change of sodium acetate

Figure 29 miniaturized mock-up demonstration with small MTC device-installed window and control units

Figure 30 Schematic model for a movement of syringe tip. Note that stored energy in the spring makes large mechanical impact instantly

Figure 31 The transmittance and haze variation with the sodium acetate phase change as liquid and solid for each chamber

Figure 32 O The cyclic test up to 200 cycles shows the durability of MTC device without significant degradation

Figure 33 A pendulum impact test

Figure 34 The logic flow chart for smart glass system integrated with MTC device and control units

Chapter 1. Introduction

1.1. Study Background

In recent decades, metal nanomaterials are widely studied for its particular physical, chemical and electrical properties such as lowered melting temperature, extremely large surface to volume ratio and ballistic transport characteristic.^{1–4} Those features of metal nanomaterial are promoted to develop novel types of electronics: transparent conductive electrode (TCE)^{5–6}, thin film transistor^{7–9}, organic light emitting device (OLED)^{10–11}, micro heater¹², solar cells¹³, sensors^{14–17} and other electronic devices. Among various metal nanomaterials, copper attracts huge attention due to its remarkable cost effectiveness as well as superior electrical/thermal conductivity than other noble metals.^{18–19} Despite several merits, the practical use of copper nanomaterials is limited because of their easy oxidation issue in ambient condition. Besides, copper nanoparticles (Cu NPs) need an additional annealing process at elevated temperature to enhance the contact resistance problem between nanomaterials for better electrical pathway. Therefore, thermal annealing process in vacuum or inert/reduction gas environment is widely adopted to minimize the oxidation for copper nanomaterials while the inert gas environment cancels the low cost advantage of using Cu nanomaterial and high

temperature thermal annealing process is hard to be applied for flexible electronics.^{20–22}

To improve those drawbacks in Cu nanomaterials, several alternative methods were suggested such as new material or an alternative low temperature annealing process. For instance, Cu nanoparticles/nanowires are synthesized and encapsulated by stable materials such as carbons, thiolated self-assembled monolayer and polymers to suppression oxidation.^{20, 23–25} Although these methods may minimize oxidation, those encapsulation materials may cause other problems such as reduced electrical conductivity and higher annealing temperature with prolonged duration for removing residuals effectively. Accordingly, intense pulsed lamp irradiation process is proposed to realize low temperature annealing without oxidation.²⁶ However, it needs predefined photomask patterns with enough working time for sintering. Meanwhile, laser-assisted process is employed due to its obvious merits including selective annealing feature for in-situ direct writing/patterning and fast working speed at ambient atmosphere without oxidation. For example, selective laser sintering/welding process is executed on metal nanomaterials for flexible applications in previous works.^{6, 27–35}

Nevertheless, the primary examination on the effect by using different thermal treatments of conventional thermal annealing with inert gas condition and selective laser sintering process in air on the nanomaterials is rarely studied yet. Moreover, the benefit of using selective laser sintering process for Cu nanomaterial is not

fully understood in aspects of material analytics. Therefore, an evaluation for the advantages of the laser sintering process is required to compare with traditional thermal annealing process. Herein, we report the various thermal behaviors including chemical, electrical and surface morphology of the sub-50 nm Cu NPs annealed by conventional tube furnace heating in Ar atmosphere and by selective laser sintering process in air. Prior to annealing process, Cu NPs are mixed with DI water and other liquids to form Cu NP paste which is a main material in this study. Thermogravimetric-differential thermal analysis (TG-DTA) is performed to show basic thermochemical activity for Cu NP paste. Moreover, the compared process and its results are inspected by using diverse analytic tools including scanning electron microscopy (SEM), transmission electron microscopy (TEM), X-ray diffractometer (XRD), Fourier transform infrared spectroscopy (FT-IR) and X-ray photoelectron spectroscopy (XPS). Finally, as a proof of concept, flexible transparent conductor and touch panel were demonstrated.

Recently, copper (Cu) nanomaterial has emerged as a promising material for functional electronics such as transparent/stretchable conductor, transistor, sensor and electrochemical cell by a novel fabrication process due to its good electrical/thermal properties and economical merits as well. 1-5 However, Cu tends to get easily oxidized and lose its electrical conductivity in the ambient condition. Nanoscale materials have extremely large surface to volume ratio, therefore, oxidation

problem will be much more severe for Cu nanomaterial compared with bulk Cu.^{6–7} In order to prevent oxidation issue, Cu nanomaterials are usually encapsulated with stable materials such as carbon nanomaterial, thiol or polymer right after synthesis.^{8–10} In addition, oxidation suppression techniques during fabrication or post-processing have been developed such as electroplating, direct printing system, intense pulsed light (IPL) sintering and selective laser sintering/welding process.^{11–15}

1.2. Purpose of Research

Although much progress has been accomplished, still several technical challenges hinder the practical use of Cu nanomaterial and development of fabrication techniques. First of all, Cu nanomaterials need to be synthesized under a precise temperature control, which make it hard to be applied for mass production.^{16–18} Considering that the Cu nanomaterial is usually solution processable, critical factors such as weight percent, surface tension and viscosity need to be optimized for direct printing methods.^{19–21} Moreover, high power lamp or laser often brings an undesirable film delamination or a surface damage.^{22–23} Recently, Mayousse et al. reported a simple glacial acetic acid (GAA) treatment on the Cu nanowire (NW) for a transparent conductive electrode.²⁴ The GAA treatment removes Cu oxides and other residues from the surface of Cu NW. PEDOT:PSS coating is followed after GAA treatment to enhance the electrical connectivity between the Cu NWs and chemical stability against the oxidation. While the GAA treatment shows facile surface treatment for the Cu NW, it requires an additional coating layer causing instability in electrical conductivity and reduced transparency.

In this research, we developed a simple and cost-effective Cu patterning method on a flexible PET film by combining a solution processable Cu nanoparticle (NP) patterning method and a low temperature post-processing. The simple patterning method of Cu

NPs enabled to minimize material waste and to enhance reproducibility of the process. Subsequently, the transferred Cu NP patterns were treated by using various post-treatment methods such as acetic acid treatment (AAT), laser sintering process (LSP) and the acid-assisted laser sintering process (ALSP). Unlike GAA treatment, the fabricated Cu patterns showed superior chemical, electrical and mechanical stability. The developed ALSP process was found to ensure much superior oxidation suppression and mechanical stability over other post-treatment methods. The ALSP treated conductive Cu electrode may have a promising applications in various flexible electronics with good reliability.

Recently, technological convergence has stimulated the appearance of evolved fields such as multi-functional smart devices.(1–3) In particular, the advanced convergence technology can provide additional functionalities to the classical tools, eventually, it reinvents or redefines old things to a revolutionary one.(4, 5) Accordingly, various techniques for imparting new functionality to the window are under active development including heatable(6), energy generation(7), anti-bacteria(8), high-scratch resistance(9) and color-switchable window. Among the techniques, the color-changeable smart window has been intensively interested due to privacy protection, artistic designs and effective energy management for the building.(10) To date, several types of smart windows have been explored such as suspended particle device (SPD)(11, 12), polymer-dispersed liquid crystal (PDLC)(13–17), electrochromic(18–21), photochromic(22, 23) and thermochromic

device.(24–27) In particular, each of smart window has unique characteristics in aspect of working principle, operation conditions and performances (Table S1). For instance, SPD, PDLC and electrochromic window commonly use electric energy to control direction of polar particles, orientation of polar molecules and electric charge transfer. While these electricity–based smart windows ensure fast color–switchable speed and high optical transmittance difference at bleached and colored state, electric energy has to be supplied to turn the device on/off.(11, 28) In case of a photochromic window, it reacts with UV from sunlight and shows a weak color switching during several minutes.(22) Meanwhile, thermochromic devices require a constant thermal energy including reflected infrared energy during daytime or electrothermal heat from the micro heater to activate and to keep its color–shifting feature. High–energy consumption for phase changeable metal oxide and low visibility for thermochromic pigment also limits their wide application.(29) In this regard, smart window based new working principle would introduce in order to bring novel applications and motivate further investigations.

Sodium acetate (CH_3COONa) is a kind of salt hydrate and it broadly used in textile industry, pH buffer solution, solar energy storage system and heating pads. Particularly, sodium acetate can contain water molecules within its crystal structure, eventually forms hydrate(30) and shows a unique heat release characteristic during crystallization from supersaturated solution. Sodium acetate can be fully dissolved in a heated deionized water to be saturated

and it becomes supersaturated after natural cooling at room temperature. However, this supersaturated state of sodium acetate solution is unstable so that the spontaneous phase change into crystalized sodium acetate trihydrate(31) and exothermic heat release occur when external mechanical stimulation is applied. Beside the heat release phenomena during phase change, sodium acetate shows distinctive optical property change. Fully dissolved or supersaturated sodium acetate is highly transparent solution while crystalized sodium acetate trihydrate is opaque milky colored crystal.

Although most of sodium acetate related researches have focused on the exothermic heat release feature by phase change, we, for the first time, demonstrated the possibility of applying sodium acetate to optical devices as a mechano-thermo-chromic (MTC) smart window. As this chemical reaction is reversible, transparent supersaturated sodium acetate solution can instantly change into murky sodium acetate trihydrate crystals upon mechanical stimulus (mechano-chromic) and the opaque murky sodium acetate trihydrate crystals can go back to transparent sodium acetate solution state again when heat is applied (thermo-chromic). Since the dissolving ratio of the sodium acetate crystal in solution significantly varies upon temperature, its solubility and transparency may be precisely adjusted by thermal control. By applying those unique optical property differences during the phase change of sodium acetate, in this study, we present a new concept mechano-thermo-chromic device that changes and maintains its

optical property by mechanical stimulus and heat. Compared to the traditional smart windows, the MTC device consists of the simplest components and enables to maintain high optical transmittance state or opaque state without constant electrical/thermal energy. The phase changeable sodium acetate is basically governed by thermal energy, which is similar to the typical thermochromic and chalcogenide materials. The chalcogenide based optical modulators show extremely fast switching speed than that of sodium acetate.(32, 33) However, unlike typical thermochromic window, the MTC device shows fast response time(25, 34), high optical switchable range(3, 27) and transient thermal energy demand for phase changing. Therefore, this new concept may provide a novel color-switchable feature for the future smart window application.

Chapter 2. Material synthesis and process setting

2.1. Copper nanoparticles synthesis

0.2 M of $\text{CuSO}_4 \cdot 5\text{H}_2\text{O}$, 0.75 M of $\text{NaH}_2\text{PO}_2 \cdot \text{H}_2\text{O}$ and 0.005 Mw of Polyvinylpyrrolidone (K-30) is dissolved in ethylene glycol at 90 °C. All chemicals are purchased from Aldrich. The synthesis reaction is finished in 15 minutes with a lab-scale quantity. The synthesized Cu NPs are cleaned with acetone, ethanol and deionized water, respectively. The size of Cu NPs are sub-50 nm and colored in deep brown. Details for the synthesis procedure is described in previous study.²⁴ Approximately 0.9 g of Cu NPs are mixed in 2 mL of DI water for 30 wt% solution. Small volume of isopropyl alcohol (IPA) and diethylene glycol is added for well-dispersed and sufficient viscosity solution. The Cu NP thin film is deposited on general slide glass substrate or 25 μm thickness of polyethylene-naphthalate (PEN) film by simple bar-coating method. An air plasma treatment is performed at 50 W for 1 minute before the bar-coating process to enhance adhesion strength between Cu NPs and substrates. The thickness of the as-prepared and the laser-sintered (red dotted box) Cu NP thin film on the glass substrate is around 11 μm and 3.2 μm , respectively (Figure S1, Supporting Information).

2.2. Selective Laser sintering

The selective laser sintering process is applied on the as-prepared Cu NP thin film to enhance the electrical conductivity without oxidation problem. The absorption spectrum of as-prepared Cu thin film on the glass substrate is represented in Figure S2, Supporting Information. Diode-pumped ND:YAG laser (Lighthouse Photonics, Sprout-D) is operated in continuous wave (CW) at 532 nm wavelength to provide a localized heat source. The laser is scanned rapidly on the sample by using 2D galvano-mirror scanner. Laser beam passes through half wave plate (HWP) and polarized beam splitter (PSB) to adjust laser power. Another beam splitter (BS) is placed afterwards to measure laser power without changing laser polarization. Because laser beam after PBS has only p-component polarization, linear polarized laser beam can be changed to circular polarized laser beam with quarter wave plate (QWP). The linearly polarized laser beam, which is polarized at $\pm 45^\circ$ with respect to the horizontal, passes through the QWP with the fast axis horizontal to change its polarization state as the following Jones matrix. To attain a rapid scan of focused laser spot on 2D plane, laser scanner (Scanlab, HurrySCAN II) is used. The laser scanner consists of 2D galvano mirrors and f-theta telecentric lens. ($f = 100$ mm, Linos) In a typical laser sintering process, the focused laser beam is raster scanned on the sample with a fixed hatch size of 5 μ m. The laser spot size for the current

optical setting is estimated to be $\sim 10\ \mu\text{m}$ in diameter, and the corresponding heating time at 100 mm/s scanning speed is as short as $\sim 100\ \mu\text{s}$ for each spot.

2.3. Cu nanoparticle mold transfer method

In order to fabricate a master mold for Cu NP patterning, a (111) silicon substrate was cleaned and photoresist patterning was done on the Si wafer by conventional photolithography. Then, Si substrate was etched by reactive ion etcher (RIE) and residual photoresist was removed by acetone. Afterward, Cu NP paste was deposited on the patterned Si master mold and the excessive Cu NP paste was removed by razor blade. Subsequently, UV curable epoxy resin (CCTECH, SEA-1) was spun on the Cu NP pasted covered Si mold and PET film was placed on top of epoxy resin, which was then cured under UV light (400 W, 350 nm) for 120 sec. After UV curing, the Cu NP patterns on Si master mold was transferred to the PET flexible substrate to make Cu NP patterns on a flexible epoxy/PET substrate.

2.4. ALSP process

Acetic Acid Treatment (AAT) and Selective Laser Sintering Process (LSP): For AAT, the acetic acid (99%) and DI water were mixed by 1:2 volume ratio. The as-prepared Cu NP electrode was

immersed in the mixture solution for 1 minute to remove the oxide and contamination on the surface of Cu NP. After the AAT process, the excess acetic acid was washed out with DI water and then it was dried in room temperature.

The selective LSP was applied on the as-transferred Cu NP thin film to enhance the electrical conductivity by sintering of Cu NPs. Diode-pumped ND:YAG 532 nm continuous wave laser (Lighthouse Photonics, Sprout-D) was applied as a localized heat source to exploit the plasmonic nanowelding between Cu NPs. The focused laser spot was scanned rapidly on the sample by using 2D galvanometer scanner (Scanlab, HurrySCAN II) and f-theta telecentric lens. ($f = 100$ mm, Linos). In a typical laser sintering process, the focused laser beam was raster scanned on the sample with a fixed hatch size of $5\text{ }\mu\text{m}$. The laser spot size for the current optical setting was approximately $10\text{ }\mu\text{m}$ in diameter. The corresponding heating time at 100 mm/s scanning speed is as short as $\sim 100\text{ }\mu\text{s}$ for each spot.

2.5. Smart glass application

Fabrication of MTC device: 140 g of sodium acetate (99%, anhydrous, Aldrich) was dissolved in 100 mL of DI water at $65\text{ }^{\circ}\text{C}$ to get a saturated solution. The sodium acetate solution cooled down to room temperature and it formed a supersaturated solution for phase transition. The PDMS (Sylgard 184, Dow Corning, 10:1

ratio of the base and curing agent) chambers were designed for various thickness chambers by different glass blocks. The transparent micro heater was fabricated by using copper nanopaste and an acid-assisted laser sintering process. Detailed information on acid-assisted laser sintering process can be found in the previous report.²⁰ The PDMS chamber and the transparent micro heater was glued together with PDMS adhesive (3140 RTV Coating, Dow Corning) for solution sealing. Then, the sodium acetate solution was discreetly injected into the PDMS chamber.

2.6. Material Characterization

The morphology of as-prepared Cu NP and annealed Cu NP thin films are observed by SEM (JEOL, JSM-7600F). The lattice structure of copper is confirmed by TEM (JEOL, JEM-3000F). A basic thermal activity of Cu NP paste is examined by TG-DTA (TA Instruments, SDT-Q600) with 100 mL/min of Ar flow rate and 10 °C/min of heating rate. Electrical property is measured and calculated by four-point probe (MSTech, M4P-302) with source meter unit (Keithley, Model-2400). The effect of thermal treatment on Cu NP thin film and polymer is analyzed by FT-IR (Bruker, Tensor 27). Crystalline phase and chemical binding energy of Cu NP thin films are obtained by XRD (Bruker, D8 Advance) and XPS (Thermo-Fisher Scientific, Sigma Probe) analysis, respectively. AFM (Nanostation II, Puco Tech) is used to display

the Surface topology of a Cu conductive line.

Cyclic Bending Test and Touch Panel Fabrication: The electrical and mechanical stability of the copper grid pattern on a PEN film is performed by cyclic bending test. The experimental setup is established by moving one end at the frequency of 1 Hz while the other end is fixed. The bending radius for the sample is only 2.25 mm at the maximum bending deformation (Movie S1. Supporting Information). The copper grid pattern on PEN film is connected with the controller. And ITO glass is selected as conductive layer for the other size of the resistive-type touch sensor.

Tube Furnace Heating: Traditional furnace heating process is performed in general tube furnace in Ar environment (99.99%) at 200 mL/min flow rate. Annealing temperature set for 400 °C for 1 hour with 10 °C/min heating rate and furnace cooling. In order to make sufficient necking points and lowering porosity for the copper thin film, relatively high annealing temperature is adopted in this study. Prior to thermal annealing process, Ar purge is executed for more than 30 minutes.

Humidity-temperature Test, Cyclic Bending Test and Touch Panel Fabrication: The electrical and mechanical stability of the fabricated Cu grid electrode on a PET film was performed by a cyclic bending test. The experimental setup was established by moving one end at the frequency of 1 Hz while the other end was fixed. The bending radius for the sample was 2.25 mm at the maximum bending deformation. The humidity-temperature test was conducted in the conventional oven within over 80 % humidity and 80 °C

environment. A resistive-type touch panel was demonstrated. The Cu grid electrode on a PET film was connected to the touch panel controller and ITO glass was used as the other electrode for touch panel.

Material Characterization: The surface morphology of sodium acetate trihydrate crystal was observed by SEM (JSM-7600F, JEOL). The optical property of MTC device was characterized with UV-VIS spectroscopy (V-770, JASCO) for transmittance and haze measurement. The performance of the transparent electro-thermal micro heater and the temperature variation with sodium acetate solution solidification were investigated with an infrared (IR) camera (A645sc, FLIR), which showed the temperature and thermal distribution with time. The transmittance changes with phase transition in real time was measured by lab-made system, which consisted of a laser, a beam expander and a photodetector. The transmitted laser power varied with the state of the transition solution on a uniform area covered by expanded laser. The MTC device on the roof of the mini model house was controlled by a microcontroller board (Arduino Uno Rev3) with the control logic.

Chapter 3. Experimental result : selective laser sintering of copper nanoparticles

3.1. Copper nanoparticles synthesis and Laser optical setting

The Cu NPs are synthesized by polyol process with lab-scale production.²⁴ Figure 1(a–b) represents SEM and TEM pictures of 45 ± 5 nm sized Cu NPs. The synthesized Cu NPs have high crystallinity with thin polyvinylpyrrolidone (PVP) layer on surface. The synthesized Cu NPs are dispersed in deionized (DI) water with additional solvent to make Cu NP paste. Subsequently, the prepared Cu NP paste is deposited onto a slide glass substrate by a simple bar coating method. For the comparison of thermal behavior, the Cu NP deposited glass substrate is annealed either by laser irradiation in air environment or by conventional tube furnace heating in air or Ar environment. A schematic of selective laser sintering system is represented in Figure 1(c) which consists of 532 nm continuous wave Nd:YAG visible laser to provide a localized heat source, 2D galvano-mirror scanner and other optics. Details for the conventional tube furnace heating condition and the configuration of the selective laser sintering system are described in the experimental section.

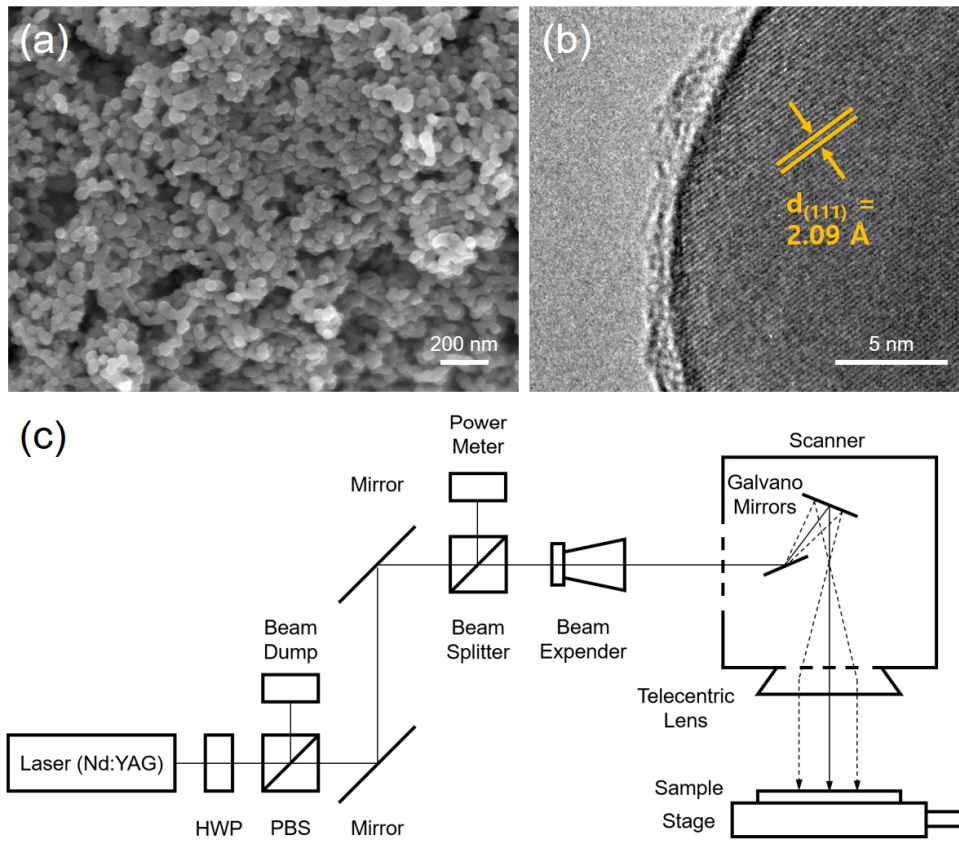


Figure 1. (a) Surface morphology and (b) crystalline structure for the as-prepared Cu NP. Individual Cu NP ($45 \pm 5 \text{ nm}$) is observed by TEM which coated with thin polymer layer for oxidation suppression. The synthesized Cu NP has good crystalline structure with lattice distance of 2.09 \AA on (111) plane. (c) Schematics of the laser sintering system.

3.2. Thermal behavior of copper nanoparticles

Prior to the thermal process, thermal characteristics and composition changes of Cu NP paste under different temperature is examined by TG-DTA. Figure 2 shows that the Cu NP paste experiences distinguished three stages up to 500 oC with 10 oC/min heating rate in thermal scanning region. At the first stage (yellow box in Figure 2), the net weight is rapidly decreased and heat flow is declined as the liquid contents off the Cu NP paste evaporates. After solvent evaporation, the PVP layer is degraded from the Cu NPs during the second stage (blue box in Figure 2). When the temperature is further increased, third stage (green box in Figure 2) shows sintering of Cu NPs at broadly around 150 - 240 oC.

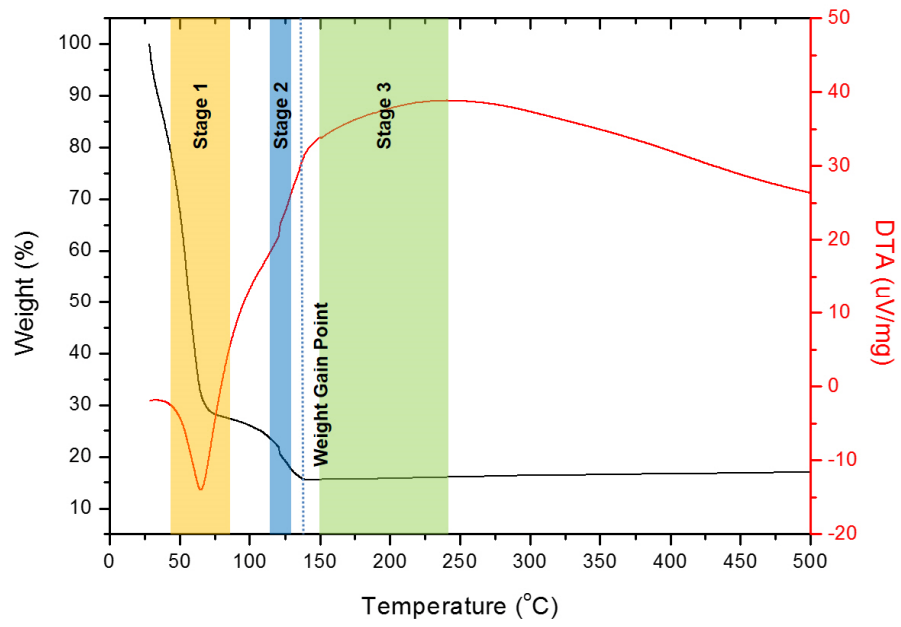


Figure 2. TG–DTA measurement for the copper nanoparticle paste up to 500 oC of temperature scanning with 10 oC/min of heating rate. The Cu NP paste shows three step transition.

3.3. Optimum condition of SLS process

Electrical property of Cu NP is measured after two different methods (tube furnace heating and selective laser sintering). The as-prepared Cu NP thin film shows low electrical conductivity due to the weak inter-nanoparticle bonding and large contact resistance. The parametric study (Figure 3(a)) on selective laser sintering process and Cu NPs is carried out to find an optimum laser sintering condition. The parametric study was conducted on the Cu NP deposited glass substrate where the active area is 4 mm² for each case as various laser power (20, 40, 60, 80 and 120 mW) and laser scanning speed (50, 100, 150, 200, 250 and 300 mm/s). The laser power at 20 mW was not sufficient for the Cu NP sintering at any scanning speed conditions (colored in white) and the sheet resistance of the Cu NP film for 20 mW laser power condition is similar to that of as-prepared Cu NP thin film. Laser sintering effect started to be observed over 40 mW laser power, however, most of the cases appeared in high sheet resistance: over 10 Ω/\square (colored in red). At 60 mW laser power, the sheet resistance drops to 2 Ω/\square (colored in yellow) with fast scanning speeds. At 80 mW and 100 mW laser power, the sheet resistance results exhibit around 1.5 Ω/\square (colored in green) with typical laser scanning speed condition. The stable sheet resistance is acquired at 120 mW with slow and intermediate laser scanning speed where the sheet resistance is below 1 Ω/\square (colored in blue). Yet, damaged region

is observed at 100 mW and 120 mW with the highest scanning speed condition (colored in black). The high-powered laser with fast scanning speed caused thermal damage for Cu NP thin film. Therefore, the optimum condition to operate selective laser sintering process for Cu NPs was found to be 120 mW of laser power and 150 mm/s of laser scanning speed in this study. By contrast, the electrical resistivity from conventional tube furnace heating in Ar environment showed a very high sheet resistance: $2.01 \times 10^4 \ \Omega/\square$, while the electrical resistivity of as-prepared Cu NPs and bulk Cu resistivity are $8.05 \times 10^7 \ \Omega/\square$ and $3.61 \times 10^{-3} \ \Omega/\square$, respectively (Figure S3, Supporting Information).

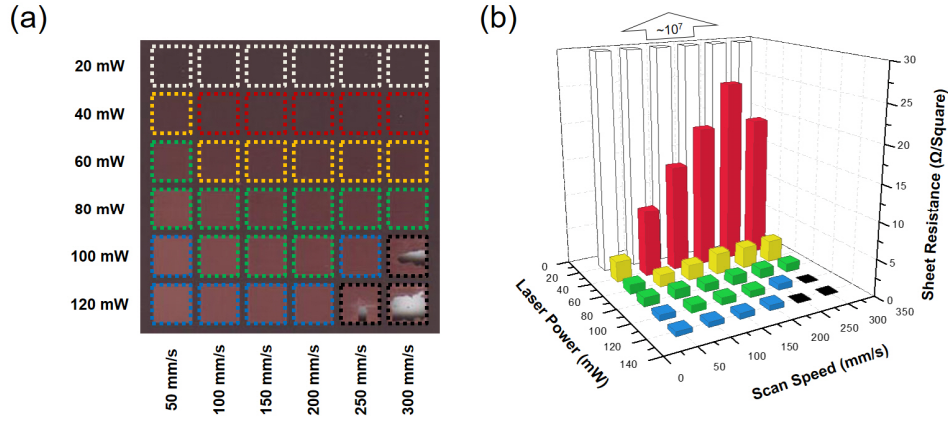


Figure 3. A parametric study on laser sintering for various laser power and scanning speed. (a) A digital picture of the results for the laser-sintered Cu NP thin film with various parametric study conditions. The sheet resistance is measured by four-point probe system and its values are represented as dotted boxes. The dot boxes are colored in white, red, yellow, green, blue and black which indicate non-sintered, over 10 Ω/\square , around 2 Ω/\square , around 1.5 Ω/\square , below 1 Ω/\square and ablation region, respectively. Note that the sheet resistance for the as-prepared Cu NP thin film and the thermal-annealed Cu NP thin film is $8.05 \times 10^7 \Omega/\square$ and $2.01 \times 10^4 \Omega/\square$, respectively. (b) A 3D bar graph represents the ranges of parametric study (XY-axis) and its sheet resistance results (Z-axis) for the Cu NP thin film. The position and color for each bar is corresponding with a dotted box on the digital picture in (a).

3.4. Comparison of thermal annealing and SLS process

Meanwhile, the surface morphology comparison of a Cu NP thin film prepared by conventional tube furnace heating and by laser sintering–processed are represented in Figure 4(a-b). The SEM image of conventional tube furnace heated Cu NPs display relatively larger particles which might be induced from particle melting. On the other hands, the laser sintered Cu NPs show closed and enlarged particle structures with reduced porosity. Those morphology images indicates the Cu NPs are sintered and can serve as a good continuous electrical pathway. Typically, the enlarged nanostructure ensures improved electrical property for conductive metal nanoparticles.^{21–22, 27} However, in this study, the Cu NPs annealing in a conventional tube furnace heater has low electrical conductivity possibly due to oxidation problem. Additionally, XRD analysis is conducted for as–prepared Cu NP film and two annealing methods (tube furnace and laser) processed Cu NP films to check their crystal phases. Figure 4(c) indicates all of the Cu NP thin films have already partially oxidized. Especially, a peak from (11–1) plane of CuO is displayed relatively high for the tube furnace heated Cu NP thin film. Both of XRD and TG–DTA results explain that residuals in Cu NP paste cause further oxidization in spite of an inert gas condition. Therefore, the Cu NPs are required to anneal within hydrogen–rich environment to supply a reducing agent for obtaining a pure Cu thin film.^{21, 36} Otherwise, the Cu thin film is

fully oxidized in air atmosphere. FT-IR analysis is conducted to realize the effect of different thermal treatment on the Cu films. Figure 4(d) suggests both tube furnace heating and laser sintering process can eliminate the polymer ingredients, e.g., the specific peak of PVP is around at 1681, 1630, 1471, 1413, 1295, 1265 and 1221 cm^{-1} of wavenumber region. Interestingly, IR spectrum of tube furnace heating in Ar environment shows peak at around 1,700 - 1,100 cm^{-1} of wavenumber region which may be related with Cu oxide families.³⁷

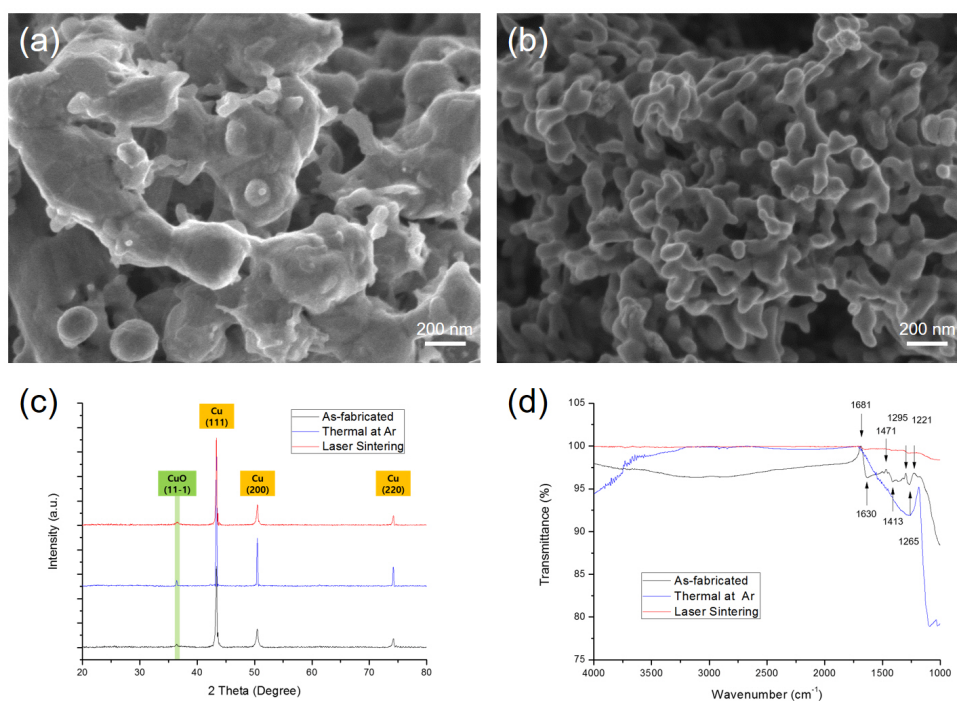


Figure 4. Comparison of Cu NP thin film surface morphology by (a) furnace thermal annealing in Ar environment and (b) by laser sintering in air. (c) XRD analysis indicates all of the Cu NP thin films have apparent Cu peaks and slightly oxidized peak. Particularly, a peak from (11-1) plane of CuO is observed relatively high for the furnace thermal annealed Cu NP thin film. (d) FT-IR result indicates composition of polymer including PVP is degraded after thermal treatment. The specific peaks for PVP is represented in the graph. Interestingly, thermal annealed Cu NP thin film exhibits strange IR peak. It is supposed to be related with peaks of Cu oxide families.

3.5. Chemical stability of Cu nanoparticles processed by thermal annealing and SLS process

The Cu NP thin films are further examined by XPS to understand its binding energy/state and chemical stability. A wide scan result of the binding energy for the Cu NP thin films is showed in Figure 5(a). Carbon peak at the 285.08 eV is selected as a reference for peak correction. All of the Cu NP thin films are observed apparent oxygen peak at 531.01 eV. The detection of the oxygen peak for the Cu NP thin films is corresponding with the results from electrical resistivity and XRD analysis. Hence, Cu NP has been slightly oxidized in every case. Selected region (colored in yellow) scan from 925 eV to 965 eV is examined to compare the chemical state and coordination bond of copper in Figure 5(b). Basically, Cu has two specific peaks with large intensity signal for Cu_{2p3/2} at around 932 eV and Cu_{2p1/2} at around 952 eV. When Cu experiences oxidation, the distance of the specific peaks closed each other. Likewise, the specific peaks will be shifted from the native position with broaden shape which indicates the changing of the coordination number for the Cu: Cu(0) → Cu(I) → Cu(II).^{38–39} Accordingly, satellite peaks appear near the each of specific peaks which implies strong evidence for the oxidation of Cu. A green box region in Figure 5(b) is replotted with separated fitting peaks of Cu_{2p3/2} family for as-prepared, tube furnace heating in Ar environment and selective laser sintering in air environment (Figure

5(c-e)), respectively. Cu_{2p3/2} peak are consists of three concealed peaks with different coordination number of Cu. In here, the Cu NP thin films of as-prepared and tube furnace heating in Ar show relatively higher side peaks of Cu_{2p3/2} signal at around 934 eV and 936 eV with satellite peaks. However, the laser sintered Cu NP thin film exhibits much more reduced signal for the side peak of Cu_{2p3/2} with weak and single satellite peak. Interestingly, the laser sintered Cu NP thin film shows weaker Cu oxidation state than other Cu thin films. This phenomena is mainly came from PVP coating layer on the surface of the Cu NP which provides oxidation suppression feature at low temperature. Since the temperature is slightly elevated, the PVP coating layer will be degraded by aqueous solutions and metal ion. Eventually, degraded PVP offers hydrogen species which plays as a reducing agent.⁴⁰⁻⁴¹ Therefore, when tube furnace heating is executed, the PVP coating layer is degraded by gradually increasing temperature in advance of sintering of the Cu NPs. While laser sintering process allows rapid temperature increase and drop, the PVP on the Cu NP can be existed until the sintering process and be acted as a reducing agent. Meanwhile, the effect of rapid laser scanning speed for the sintering of Cu NPs is a considerable factor in this study. When the laser beam with high scan speed is induced, the laser light instantly melts the surface of Cu NPs and it will stick together with fast cooling. This event is occurred at a brief instant. In contrast, the laser beam with slow scan speed meets Cu NPs, it melts the surface and inner structure of Cu NPs. Moreover, the generated thermal heat stays

longer and brings relatively large oxygen-contactable situation. Typically, the high temperature environment leads high rate of oxidation. Consequently, the laser sintering process ensures an enhanced chemical stability and oxide suppression character in ambient atmosphere.

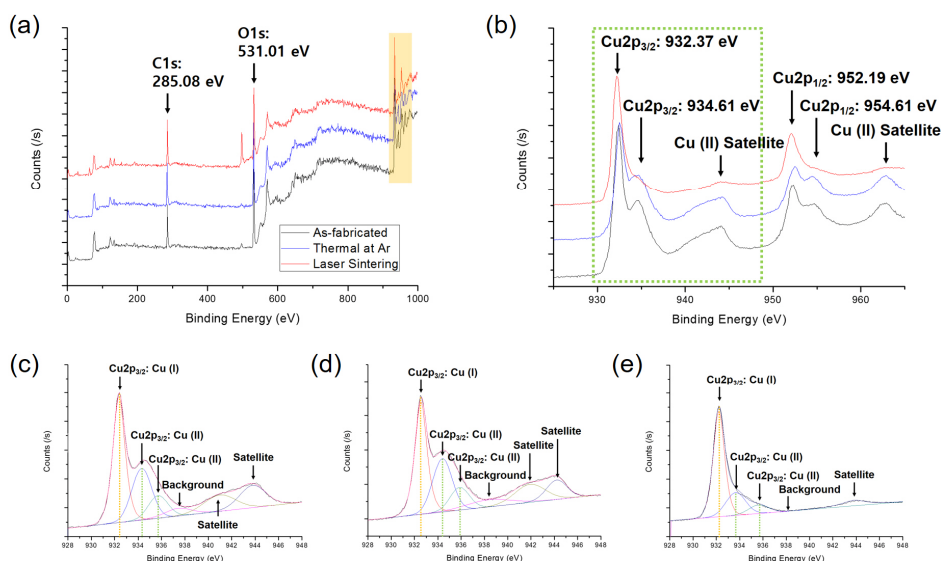


Figure 5. Comparative study on the XPS analysis for the as prepared (black line), furnace thermal annealing (blue line) and laser sintered (red line) Cu NP thin films. (a) Wide scan results is indicated that all of the samples have significant carbon and oxygen peaks at 285.08 eV and 531.01 eV, respectively. Carbon peak is used as a reference peak for peak correction. Oxygen peak implies Cu is partially oxidized. Cu-related peak are laid in yellow-colored region. (b) Cu consists of two specific peaks: Cu2p_{3/2} at around 932 eV and Cu2p_{1/2} at around 952 eV. The specific peaks are observed with slightly broaden peak profile and satellite peaks. A green box area is replotted with fitting peaks for (c) as-prepared, (d) furnace thermal annealing in Ar environment and (e) laser sintering in air environment of Cu NP thin films, individually. The Cu NP thin films of as-prepared and furnace thermal annealing in Ar show relatively high signal for the side peaks of Cu2p_{3/2} with satellite peaks. However, the laser sintered Cu NP thin film exhibits

much more reduced signal of the side peak of Cu₂p_{3/2} with weak and single satellite peak.

3.6. Flexible and transparent conductor with SLS process

The Cu NP paste is deposited onto polyethylene-naphthalate (PEN) film by bar coating method to show its applicability for flexible transparent conductor applications. The Cu NP-deposited PEN film is patterned by selective laser sintering process with condition of 60 mW and 150 mm/s. (Figure S4, Supporting Information) The dimension of grid pattern is 40 mm x 40 mm. Figure 6(a-c) represents a flexible and transparent conductor grid pattern on PEN film with 20 μm of line width (Figure S5, Supporting Information). The non-laser irradiated Cu NPs are easily washed away with deionized water shower. The fabricated Cu transparent conductor line is observed clear surface and moderate uniformity after cleaning process. The electrical resistivity of laser-sintered and non-laser irradiated Cu NP thin film is calculated to be $1.67 \times 10^{-4} \Omega \cdot \text{m}$ and $3.32 \times 10^6 \Omega \cdot \text{m}$, respectively (Figure S6, Supporting Information). Cyclic bending test also conducted at the frequency of 1 Hz up to 1,000 cycles to show electrical and mechanical stability of Cu grid pattern on PEN film. While the changing rate of the relative electrical resistance is measured $\pm 10 \%$ during the bending test, the intermediate value of the changing rate for the relative electrical resistance is less than 5% in Figure 6(d). The simple tape test is carried out to examine the adhesive strength between the laser-sintered Cu NPs and PEN

film. It shows moderate adhesive strength against a commercial adhesive tape for 60 mW, 150–200 mm/s condition after the tape test. (Figure S7, Supporting Information). Subsequently, the Cu grid pattern on PEN film is demonstrated as a touch panel (Movie S2, Supporting Information). The Cu transparent conductor grid pattern is connected to a controller and its operation is confirmed by writing the letters “ANTS” on the screen, as shown in Figure 6(e) for a practical flexible electronics application.

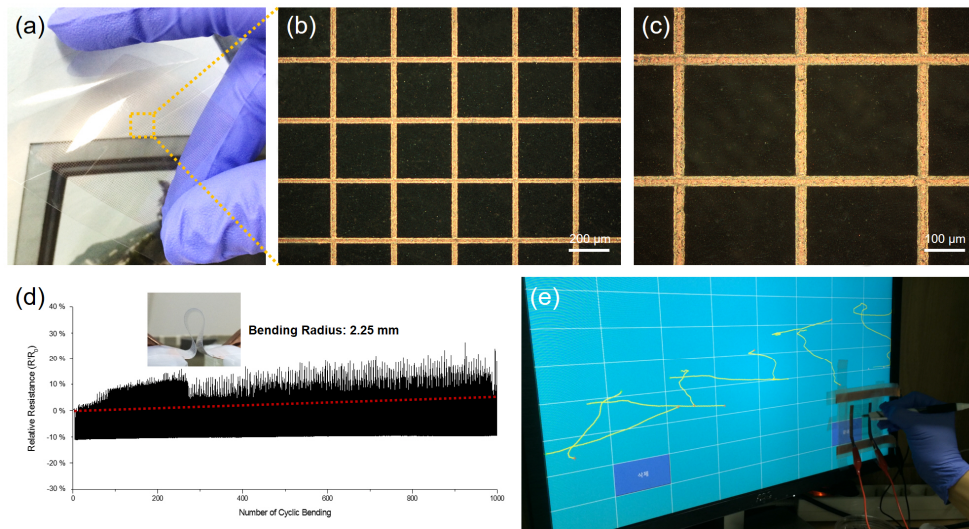


Figure 6. Flexible Cu grid transparent conductor on the PEN film by selective laser sintering of Cu NPs. (a–c) Digital images of Cu grid transparent conductor. The dimension of the grid pattern is 40 mm x 40 mm with high transparency. (d) The cyclic bending test up to 1,000 cycles to show electrical and mechanical stability. The Cu grid pattern shows $\pm 10\%$ electrical resistance changing rate with bending radius of 2.25 mm. (e) A touch panel demonstration with the Cu grid pattern on PEN film.

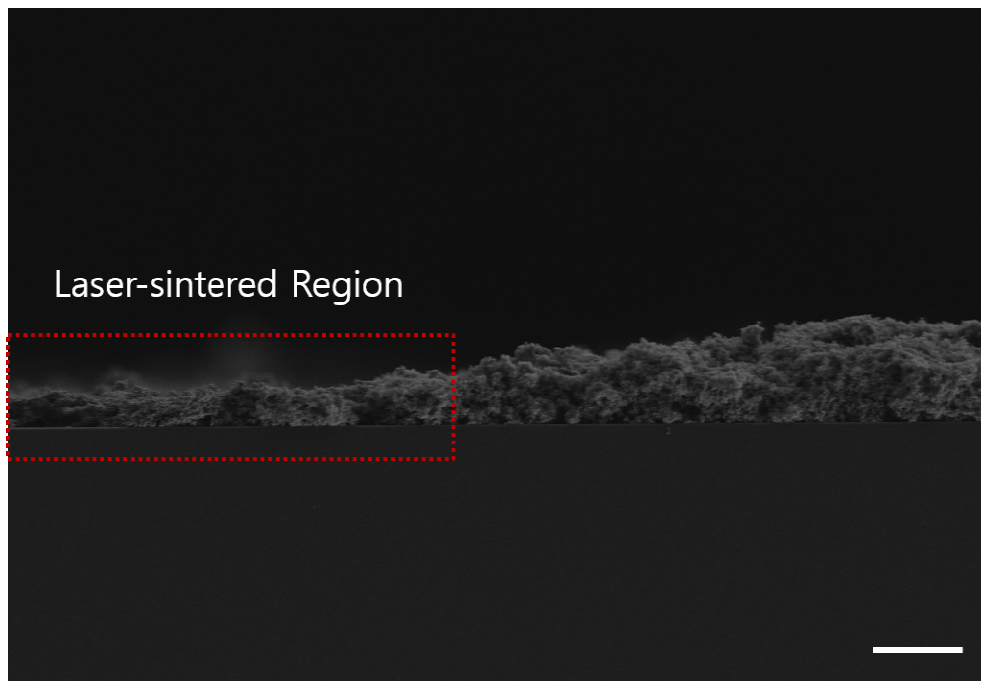


Figure 7. The thickness of the laser-sintered and non-sintered copper thin film on the glass substrate is presented. The laser-sintered region shows dense and shrinkage structure than the non-sintered copper region. Note that the scale is 10 μm .

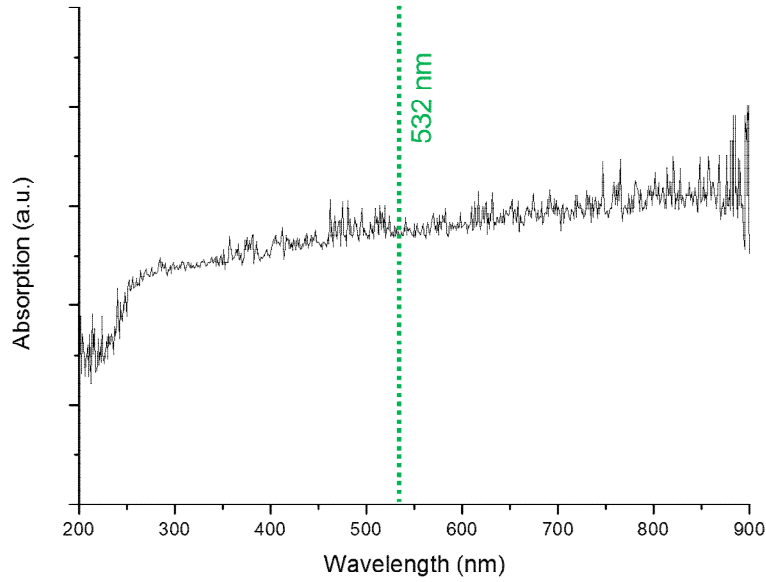


Figure 8. The absorption spectrum of as-prepared Cu thin film on glass substrate. The absorption rate of as-prepared Cu thin film on glass substrate at 532 nm is slightly lower than that of 600–800 nm. Oh et al. reported similar spectrum graph of Cu thin film in their study.¹ Generally, copper absorbs infrared wavelength region at around 600–800 nm.^{2–4} Accordingly, the 532 nm CW laser system is known as an improper laser wavelength for sintering of Cu NPs. Nevertheless, the visible-based laser system showed good performance for sintering of Cu NPs in this study. Therefore, the sintering phenomenon is not mainly caused by optical penetration depth but thermal heat transfer.

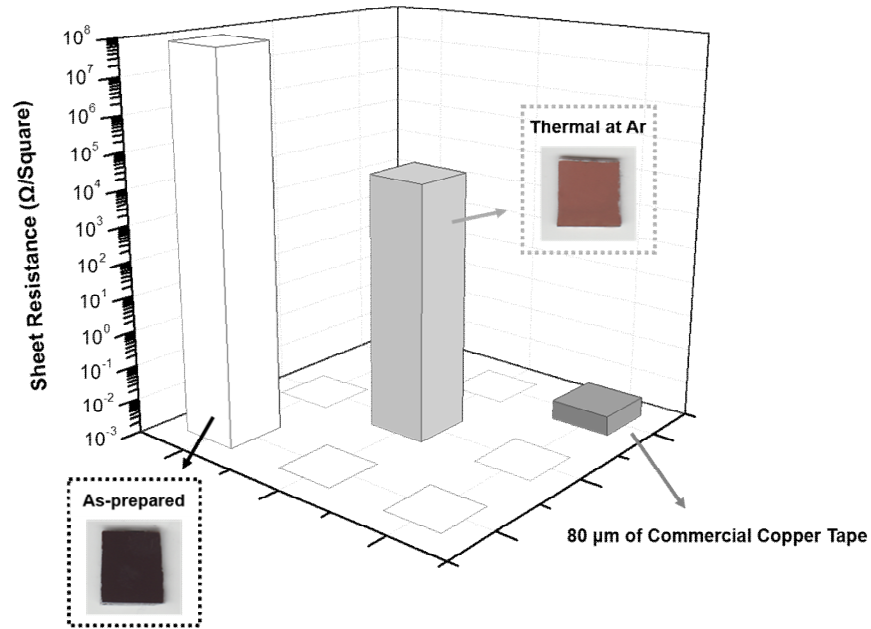


Figure 9 The compared sheet resistance of the copper samples. The sheet resistance is measured as $8.05 \times 10^7 \Omega/\square$ for as-prepared, $2.01 \times 10^4 \Omega/\square$ for thermal at Ar and $3.61 \times 10^{-3} \Omega/\square$ for commercial copper tape (thickness: $80 \mu\text{m}$), respectively.

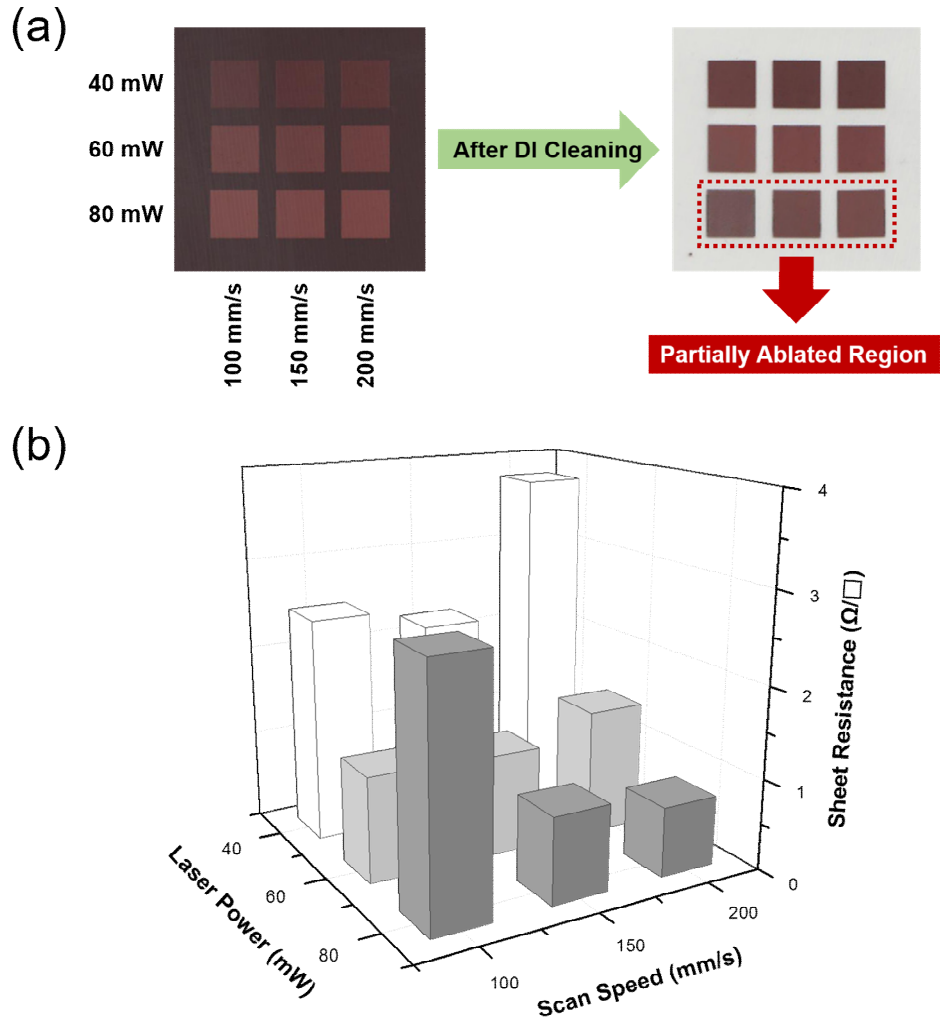


Figure 10. A simple parametric study on the laser sintering for laser power and scan speed. (a) A digital picture of the results for the laser-sintered Cu thin film on the PEN substrate. The laser sintered region shows moderate adhesion strength after cleaning process. (b) A 3D bar graph indicates the ranges of parametric study (XY-axis) and its sheet resistance (Z-axis). The position is corresponding with the digital picture in (a). The finest laser condition on the PEN film is 60 mW and 150–200 mm/s. While the sheet resistance at 80 mW and 150–200 mm/s shows lower value

than that of 60 mW, the laser power of 80 mW causes a slight ablation effect to the surface of the Cu thin film. Therefore, this laser power condition cannot be applied to make narrow line patterns for the transparency electrode.

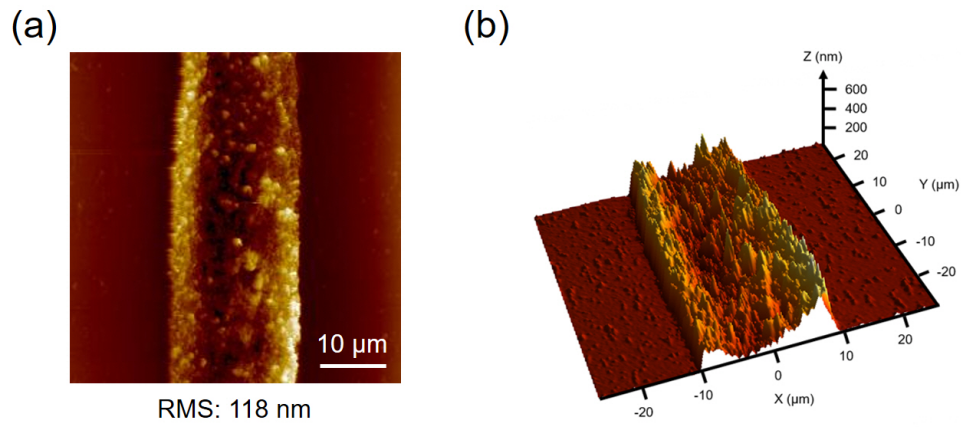


Figure 11. The topological AFM images of the laser-sintered Cu conductive line on PEN film. (a) Top-view and (b) 3D image. The RMS roughness is quite high due to the size of the pristine Cu nanoparticles. Additionally, the center region of the line is slightly damaged or concaved structure by the Gaussian property of a laser beam.

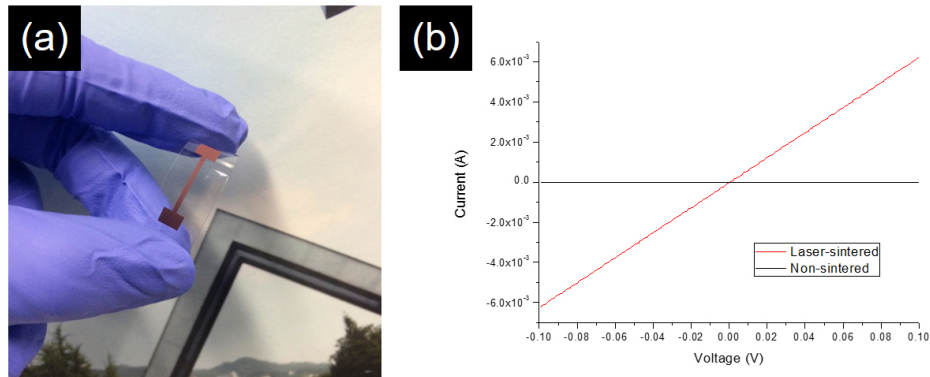


Figure 12. (a) Designed simple Cu pattern sample and (b) Electrical resistivity of before/after laser sintering process on the sample. The electrical resistivity of laser-sintered and non-sintered copper thin film is calculated almost $1.67 \times 10^{-4} \Omega \cdot \text{m}$ and $3.32 \times 10^{-4} \Omega \cdot \text{m}$, respectively. Note that the electrical resistivity is measured/calculated by following method. A sample was fabricated by using laser sintering process on PEN film. The sample is designed to have a single line with two pads at the line end. Ag paste is used on the Cu pads to improve a point of contact with measuring unit. The dimension of the sample is 4 mm x 4 mm for pad and 15 mm (W) x 1 mm (L) x 1 μm (This is a maximum value for the thickness of Cu on the PEN film, measured by AFM) for line. The calculation of electrical resistivity is: measured $R \times W \times \text{thickness} \times 1/L$.

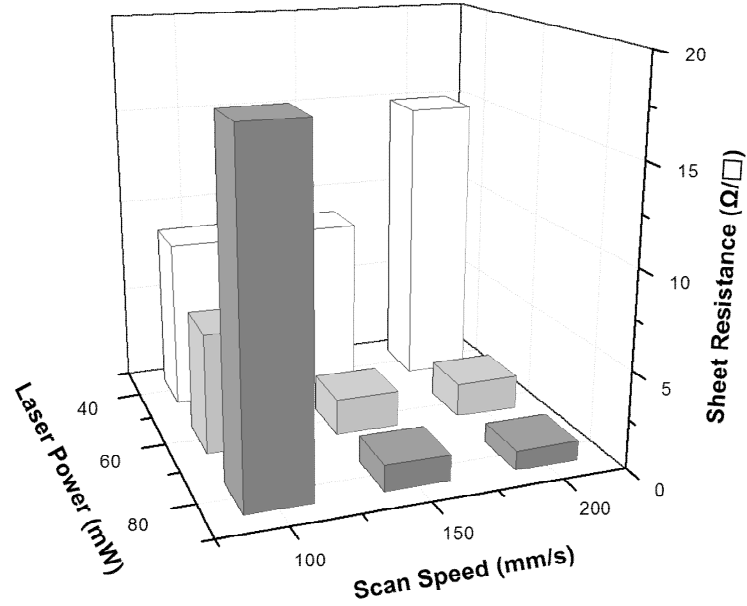


Figure 13. Tape test results for the selective laser sintered Cu thin film on the PEN film. A 3D bar graph represents the ranges of the parametric study (XY-axis) and sheet resistance (Z-axis) after a single tape test. The adhesion strength between Cu thin film and PEN substrate is comparable to the adhesive tape for 60 mW, 150–200 mm/s condition. Note that the adopted commercial adhesive tape is 3M Scotch™ magic tape, No. 810 which adhesive strength to steel is approximately 2.737 N/cm.⁵

Chapter 4. Experimental result : acid-assisted laser sintering process (ALSP) of copper nanoparticles

4.1. Mold transfer process

Cu NPs were synthesized by a modified polyol process and prepared as a paste and then bar-coated to form Cu NP thin films or patterns, which were finally transferred to the flexible substrate. Figure 1(a) represents the procedures of Cu NP patterning and transfer to the flexible plastic substrate. The Si master mold for Cu NP patterning was fabricated by using RIE with 20 μm line width (Figure 1(b)). Cu NP paste was spread and filled into the patterns on the mold and excessive Cu NP paste was removed. Then, UV-curable epoxy resin was deposited on Cu NP filled mold via spin coating.²⁶ Subsequently, a PET flexible film was placed onto the epoxy resin coated on Cu NP patterns on a mold. The epoxy resin was hardened after UV illumination to help the transfer of Cu NP patterns to a PET substrate with enhanced adhesion. The line width of transferred Cu NP electrode was same with that of the master mold as shown Figure 1(b,c).

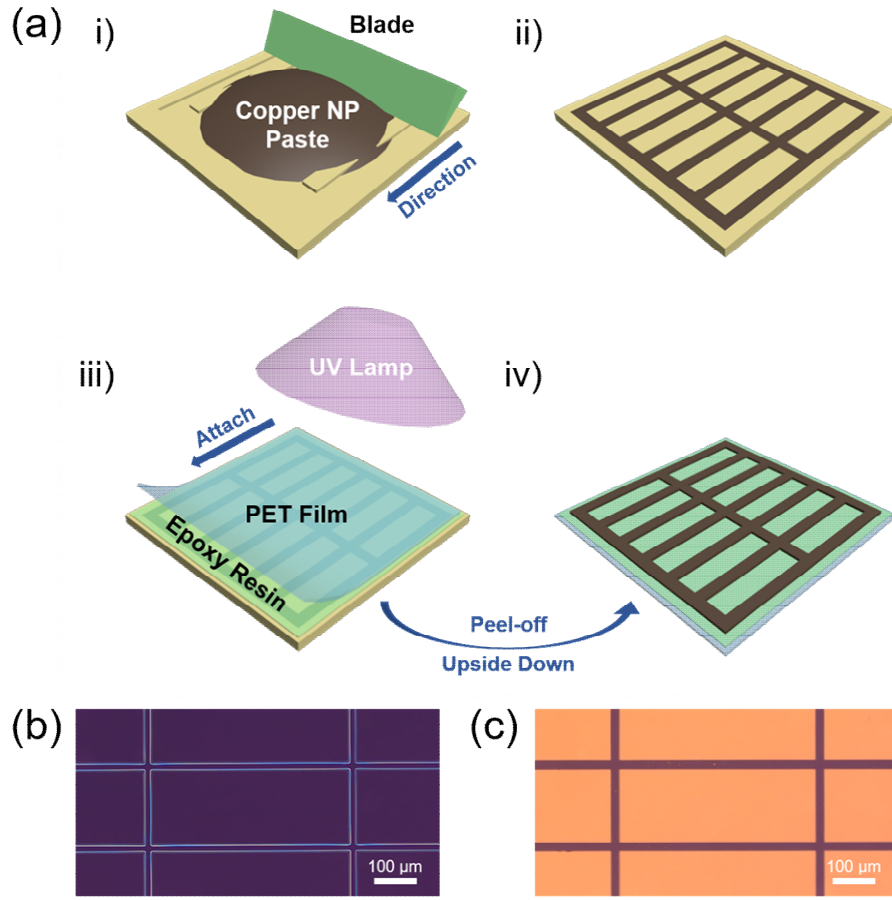


Figure 14. (a) Schematic illustration of the Cu NP patterning and transfer to the flexible substrate. (i, ii) Cu NP paste is uniformly filled in the trench of Si master mold and excessive NPs are removed by a doctor blade method. (iii) The UV-curable epoxy resin spin-coated and a PET substrate placed onto the epoxy resin. The epoxy is hardened under UV lamp irradiation to promote the adhesion. (iv) A film of copper/epoxy/PET is peeled-off from the master mold. Optical microscope image of (b) the Si master mold pattern (20 μm line width) and (c) corresponding transferred Cu NP patterns on a polymer substrate.

4.2. Post process (AAT, LSP, ALSP)

The transferred Cu NPs need a thermal annealing step to enhance the electrical conductivity and mechanical stability as well. However, conventional thermal annealing can not be directly applied because flexible polymer substrate can be thermally degraded. The Cu NP patterns were treated through combination of two kinds of low temperature post processing methods to enhance electrical conductivity without thermal damage to the polymer substrate. Figure 2(a) illustrates the post processing methods for only acetic acid treatment (AAT), only laser sintering process (LSP) and combined acetic acid treatment and laser sintering (acid-assisted laser sintering process (ALSP)). The SEM pictures (Figure 2(b)) show the different surface morphology for (i) as-prepared, (ii) AAT processed, (iii) LSP treated and (iv) ALSP treated Cu NP patterns. Right after Cu NP pattern transfer, individual Cu NPs (40 nm diameter) still showed original Cu NP shape with smooth surface (Figure 2(b)-i). However, the Cu NP surface was changed dramatically after various post-treatments. The AAT removed the oxide layer on the Cu NPs and made the Cu NP surface rough and slightly enlarged (Figure 2(b)-ii). Since the LSP provides effective melting of Cu NPs, individual Cu NPs were fused to make a continuous thin film (Figure 2(b)-iii). Combined post process of ALSP induced more complete fusion of Cu NPs to make a more smooth surface with lower porosity than LSP and AAT.

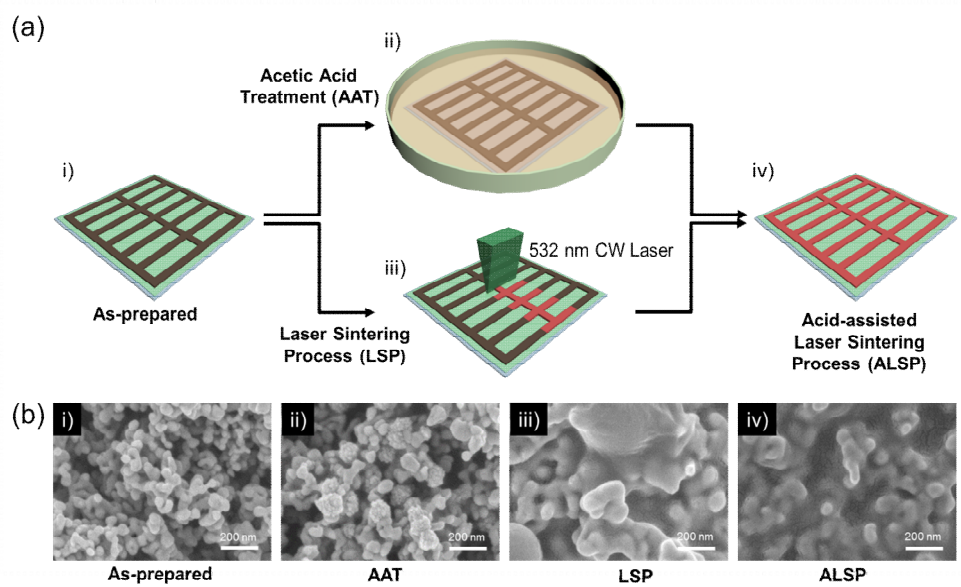


Figure 15. (a) A schematic illustration of the post-processing methods for acetic acid treatment (AAT), laser sintering process (LSP) and acid-assisted laser sintering process (ALSP). (b) SEM pictures for surface morphology of (i) as-prepared, (ii) AAT, (iii) LSP and (iv) ALSP-processed Cu NP. The Cu NP with ALSP shows compactly fused surface and low porosity structure.

4.3. Optimum condition of ALSP

For the successful laser sintering process, parametric study on the laser condition was carried out to achieve high electrical conductivity. The Cu NP paste was deposited onto a PET substrate by spin coating. To compare the effect of laser sintering with other post-treatment methods, the Cu NP thin film went through different post-treatments; AAT, LSP and ALSP. First, the sheet resistance of the as-prepared Cu NP thin film without any post-treatment was approximately $1.62 \times 10^8 \text{ } \Omega/\text{sq}$. The sheet resistance was dramatically dropped to the $42.8 \text{ } \Omega/\text{sq}$ after AAT for only 1 minutes dipping in acetic acid solution (Supplementary Figure S1). Laser parametric study was conducted on both as-prepared Cu NP thin film and AAT-processed Cu NP thin film to find an optimum laser sintering condition for each case. The laser power was varied for 20, 40, 60, 80 and 100 mW and laser scan speed was varied for 50, 100, 150, 200 and 250 mm/s. Figure 3 shows digital images of the as-prepared Cu thin film (Figure 3(a)) and AAT-processed Cu thin film (Figure 3(c)) after the laser parametric study along with 3D bar graph of corresponding sheet resistance. The boxes with colored solid lines indicate the range of sheet resistance (red: over $10 \text{ } \Omega/\text{sq}$, yellow: over $2 \text{ } \Omega/\text{sq}$, green: over $1 \text{ } \Omega/\text{sq}$, blue: under $1 \text{ } \Omega/\text{sq}$, black: $\infty \text{ } \Omega/\text{sq}$) and the dotted boxes represent damaged surface due to excessive laser energy. The sheet resistance decreased with higher laser power and slower scan speed. The

effective laser power condition is around 60 mW for both cases. However, slightly different trend was observed. In case of LSP, the sheet resistance of laser power at 20 mW was larger than 10 Ω/sq through the measured laser scan speed. At 40 mW and 60 mW laser power, the sheet resistance varied for 1–3 Ω/sq and around 1 Ω/sq respectively through the measured laser scan speed. At high laser power (80 and 100 mW), sheet resistance increased due to thermal damage on the polymer surface. Particularly, the severely damaged Cu surface and burned PET substrate were observed at 100 mW and 50 mm/s condition. In contrast, in case of ALSP, the sheet resistance was generally lower than that of LSP. The sheet resistance that could be obtained at 20 mW laser power for ALSP could be obtained at 40 mW laser power for LSP. Likewise, same sheet resistance could be obtained for 40 mW ALSP and 60 mW LSP. Over 80 mW laser power, the polymer substrate was damages. The AAT process lowers the laser power threshold for Cu NP thin film on a PET film. Since the optimum laser condition was found to be 60 mW for both LSP and ALSP, the laser operation condition was fixed as 60 mW, 150 mm/s in the following characterization study.

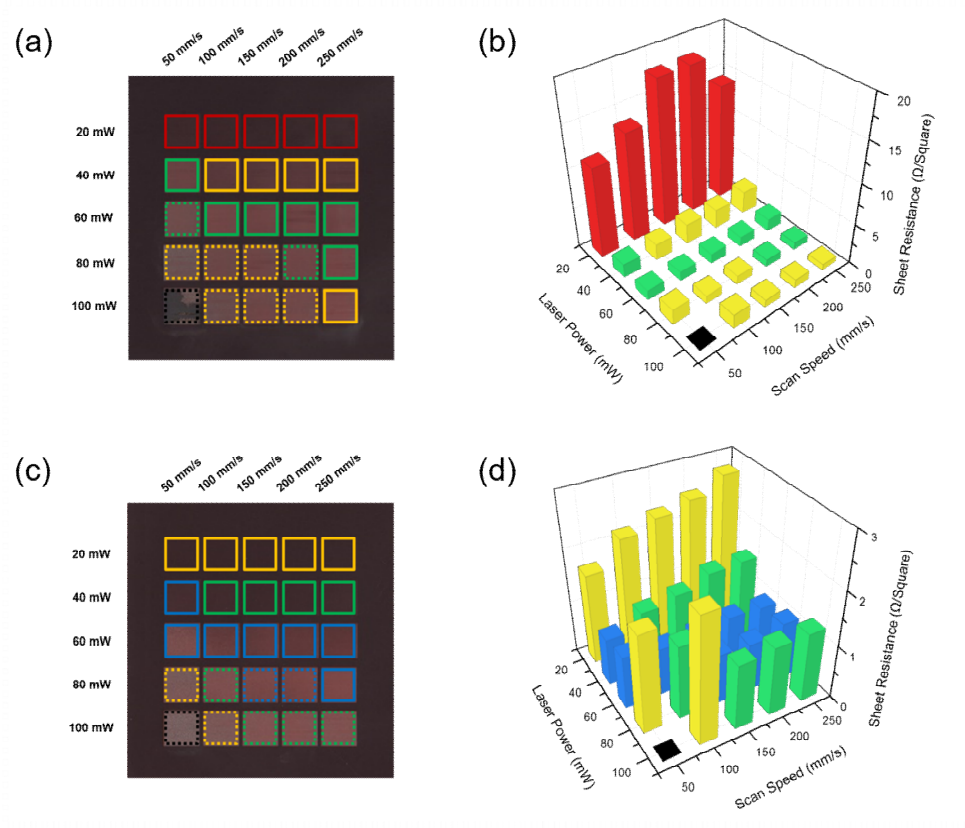


Figure 16. Parametric study on the laser sintering process for laser power and scanning speed to find optimum condition of the electrical conductivity and surface morphology. Digital pictures shows the results for the laser sintering process on the (a) as-prepared and (c) AAT processed Cu NP thin film with various laser conditions. The colored boxes show the range of sheet resistance (red: over 10 Ω/sq , yellow: over 2 Ω/sq , green: over 1 Ω/sq , blue: under 1 Ω/sq , black: $\infty \Omega/\text{sq}$) and the dotted boxes represent damaged surface. (b, d) A 3D bar graphs indicate the ranges of parametric study (XY-axis) and its measured sheet resistances (Z-axis) for the corresponding (b) LSP and (d) ALSP treated Cu NP thin film.

4.4. Chemical electrical and mechanical stability

The electrical and mechanical stability tests of fabricated Cu electrodes on PET film after each post treatment methods are shown in Figure 4. The post-treated Cu samples were exposed in ambient condition up to 2 weeks to track its sheet resistance changes due to oxidation (Figure 4(a)). The normalized sheet resistance of AAT sample showed a much steeper increase than LSP and ALSP samples, which indicates the faster oxidation rate for AAT sample. The mechanical reliability of the fabricated Cu electrode was checked by a cyclic bending test (Figure 4(b)) up to 4,000 cycles at bending radius of 2.25 mm. The normalized resistance of AAT sample could not be measured after 1,100 cycles due to electrode failure during the cyclic bending test. A case of LSP represented moderate stability up to 4,000 cycles. However, significant noise signals were also detected as compared with ALSP. The normalized resistance of ALSP showed very stable values compared with other post-processing methods throughout the cyclic bending test (Supplementary Figure S2). Additionally, a simple tape test was carried out to examine the adhesion strength between Cu electrode and the substrate in Figure 4(c). The AAT-processed Cu film exhibited an inferior adhesion and was damaged after two times tape test. The LSP-treated Cu film also showed weaker adhesion strength and the normalized resistance gradually increased after four times tape tests. On the other hand, ALSP

showed superior reliability compared with AAT and LSP during the tape test. Lastly, the humidity–temperature test was tried to find the chemical stability in a harsh condition at high humidity (over 80 %) and 80 ° C temperature. As shown in Figure 4(d), LSP and ALSP treated Cu films presented stable sheet resistance value for 1,200 seconds while AAT processed Cu film showed a dramatic increase in the sheet resistance and a break point after only 500 seconds. This signifies that the acid treatment helps to remove oxides or contaminations from the surface of Cu NP but causes serious damages on the surface morphology of Cu NP as well as a protective polymer layer, which provides oxidation inhibition property. Consequently, the chemical stability of only AAT processed Cu thin film was degraded. While the LSP treated Cu thin film presents good air, humidity and temperature stability, it showed a weak adhesion strength. Therefore, an insufficient adhesion strength to the substrate brings poor mechanical stability with scattered noise signals during the cyclic bending test. ALSP found to improve the weaknesses from other post–treatment methods. The surface of Cu NPs without oxides and polymer layer after AAT process reduces the required laser processing energy and its coupled effect resulted in densified surfaces during the ALSP treatment with enhanced adhesion strength to the flexible substrate.

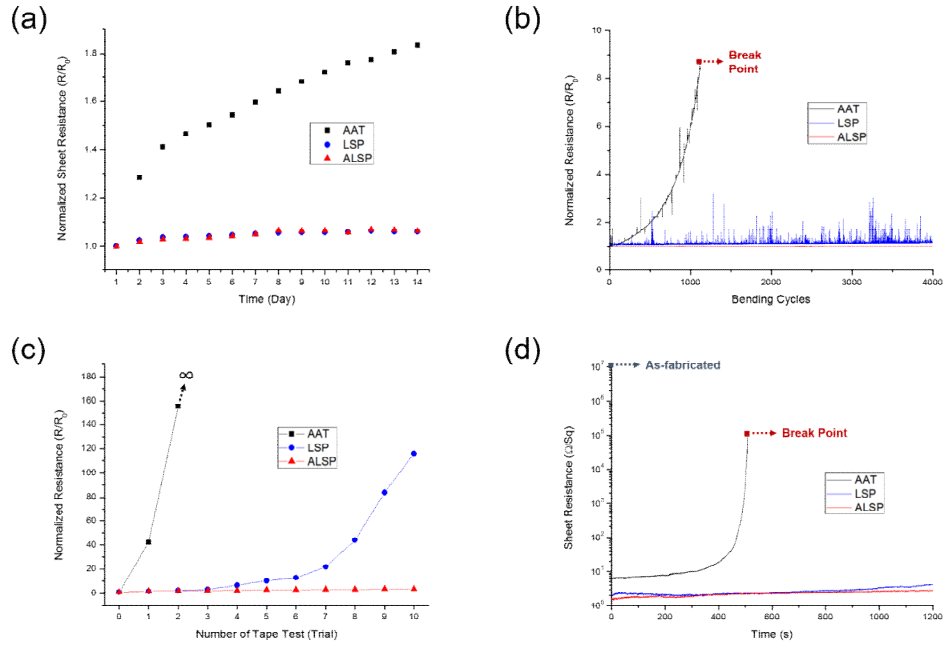


Figure 17. The chemical, electrical and mechanical stability test of Cu electrodes for various post treatment methods. Transient sheet resistance changes are measured by (a) exposure in ambient condition up to 2 weeks, (b) cyclic bending test, (c) tape test up to 10 times trials and (d) high humidity–temperature test at 80 ° C (over 80%) for 1200 seconds.

4.5. XPS analysis with process (AAT, LSP, ALSP)

To understand its chemical stability before and after humidity–temperature test, XPS analysis was conducted on the Cu electrodes after various post treatment methods (Figure 5). Typically, Cu consists of two significant peaks of Cu 2p_{3/2} at around 932 eV and Cu 2p_{1/2} at around 952 eV, respectively. Degradation of Cu can be noticed by shifting position of the significant peak with a generation of a satellite peak, related with a coordination number of Cu.^{27–28} As initially, the Cu NPs are slightly oxidized, which originated from the synthesis sequence (Supplementary Figure S3) A strong specific peak without any satellite peak around 932 eV was observed from the Cu electrodes with AAT, LSP and ALSP treatment in Figure 5(a–c). During the humidity–temperature test, hidden Cu2p_{3/2} family peaks at around 934 eV and 936 eV appeared from samples of AAT and LSP treatment in Figure 5(d–e). An appearance of family peaks implies Cu changed its coordination number from Cu (I) to Cu (II), which eventually resulted in oxidation.²⁹ ALSP treated Cu film showed good chemical stability against harsh condition while AAT and LSP treatment were degraded in Figure 5(f). A major reason of this difference originates from the post treatment methods. The acid treatment exposes pure Cu surface by removing oxides and other contaminations. Cu has higher thermal conductivity and lower specific heat capacity than Cu oxides.^{30–31} However, the only acid

treated Cu electrode cannot remain stable because the contact points between NPs are loose in this case without thermal annealing. While the laser sintering provides enhanced chemical, electrical and mechanical stability, it requires relatively high energy for processing. Likewise, this can be supported by XRD analysis. The as-prepared Cu NP electrode was slightly oxidized with Cu₂O peaks. The Cu₂O peaks disappear after AAT process and the following ALSP treatment. In contrast, Cu electrode with LSP showed strong Cu₂O peaks. After the humidity-temperature test, all Cu electrodes are oxidized. However, relatively lower Cu₂O peaks were observed in ALSP-treated Cu electrode (Supplementary Figure S4). Therefore, ALSP could achieve denser film structure and improved adhesion strength since the thermal heat from the laser can directly penetrate to the Cu surface.

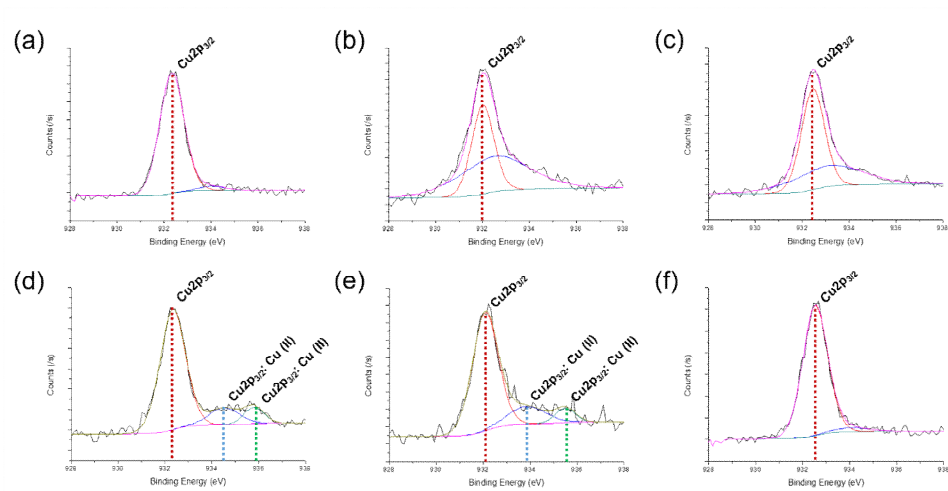


Figure 18. XPS characterization is verified on the Cu electrode after various post-treatment methods for (a) AAT, (b) LSP and (c) ALSP. The Cu peak of Cu2p3/2 at around 932 eV shows moderate chemical state of Cu for the all samples. The chemical stability of the Cu samples is observed by humidity-temperature test. After a humidity-temperature test, significant peaks of Cu2p3/2 at around 934 eV and 936 eV were detected, which indicate oxidation of Cu in (d) AAT and (e) LSP. While the ALSP treated Cu sample represents high chemical stability after humidity-temperature test in (f).

4.6. Stable Joule heater demonstration

As a proof of concept, the fabricated ALSP treated Cu electrodes were applied for various applications. Firstly, the ALSP treated Cu electrode was used as a transparent and flexible Cu Joule heater. The size of the heater is 2.5 cm x 2.5 cm and its sheet resistance is 16.22 Ω/sq . As shown in Figure 6, the heating temperature can be controlled by changing applied voltage. The applied voltage increases from 1, 2, 3, 4 to 5 V, which corresponding to generate temperature is approximately 29, 38, 57, 79 and 109 ° C. An inset picture shows a digital image of the flexible and transparent Joule heater with approximately 85% transparency. The stability of fabricated transparent and flexible Cu heater was tested at various applied voltage before and after humidity–temperature test and it showed almost no change with good electrical and thermal stability. Secondly, the fabricated Cu joule heater was used to dry out the paper electronics used in a humid or wet environment (Figure 7(a)). A patch of paper tape was attached to the ALSP treated flexible and transparent heater and water droplets were applied on paper till the paper became fully wet. 4 V was applied to the Cu heater and the water totally evaporated from the paper after 10 minutes heating. The evaporation of water was monitored by checking the weight loss of water. The flexible Cu heater are flexible and can be applied for non–flat surface as shown in Figure 7(a)–v. Thirdly, the ALSP treated Cu flexible and

transparent conductor was used as a transparent conductor for a touch screen panel. The Cu transparent and flexible conductor based touch panel showed good operation even after humidity-temperature test. Therefore, the ALSP treated conductive Cu electrode may have a promising applications in various flexible electronics with good reliability.

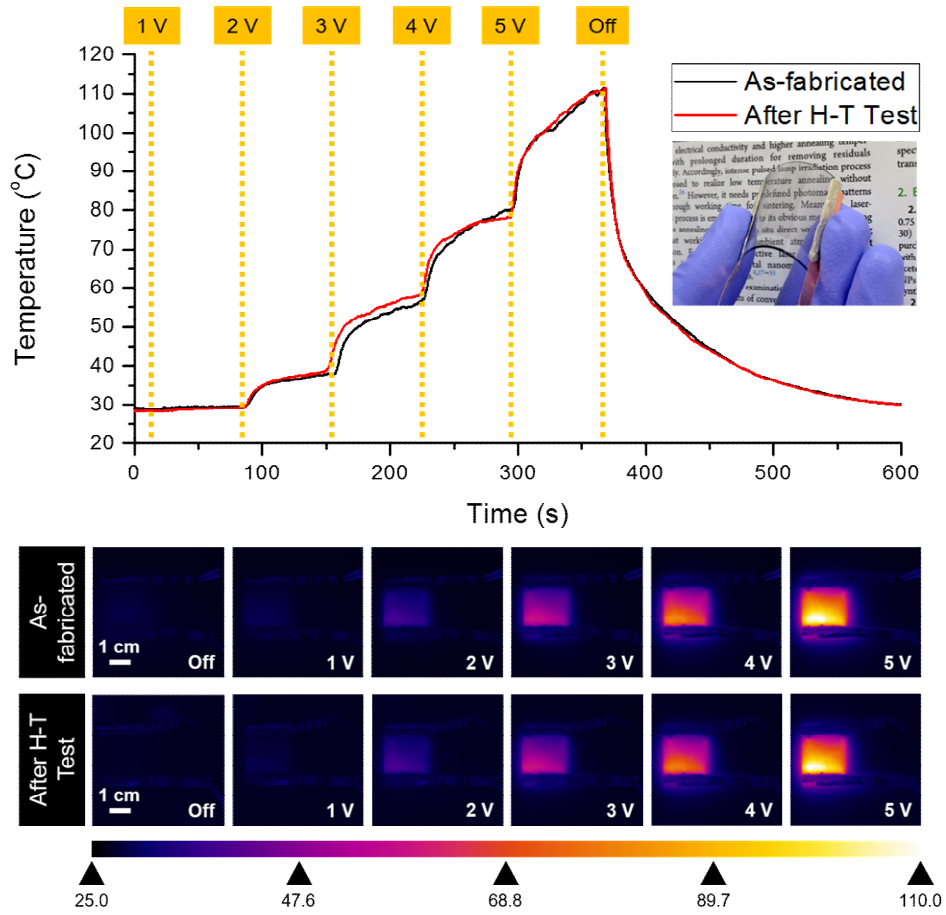


Figure 19. Transparent and flexible Cu Joule heater demonstration. Transient temperature measurement of the transferred and ALSP treated Cu electrode under increasing voltage condition from 1 to 5 V. The temperature distribution of the Joule heater is obtained by an infrared camera. The performance of the generated temperature is almost same before/after humidity–temperature test. An inset picture represents a digital image of the flexible and transparent Joule heater. Note that the transparency of the heater is approximately 85%.

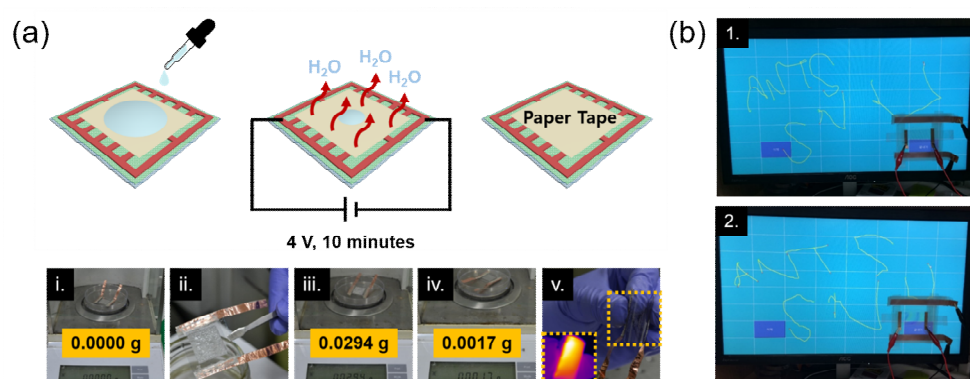


Figure 20. Applications in flexible electronics. (a) A schematic of a flexible heater/drier with wet paper tape. (i–iv) The wet paper loses its water weight after 10 minutes with 4 V of applied voltage heating condition. (v) The transferred Cu electrode successfully works as a transparent and flexible heater while bending. (b) The ALSP treated Cu electrode based touch screen panel before and after humidity–temperature test.

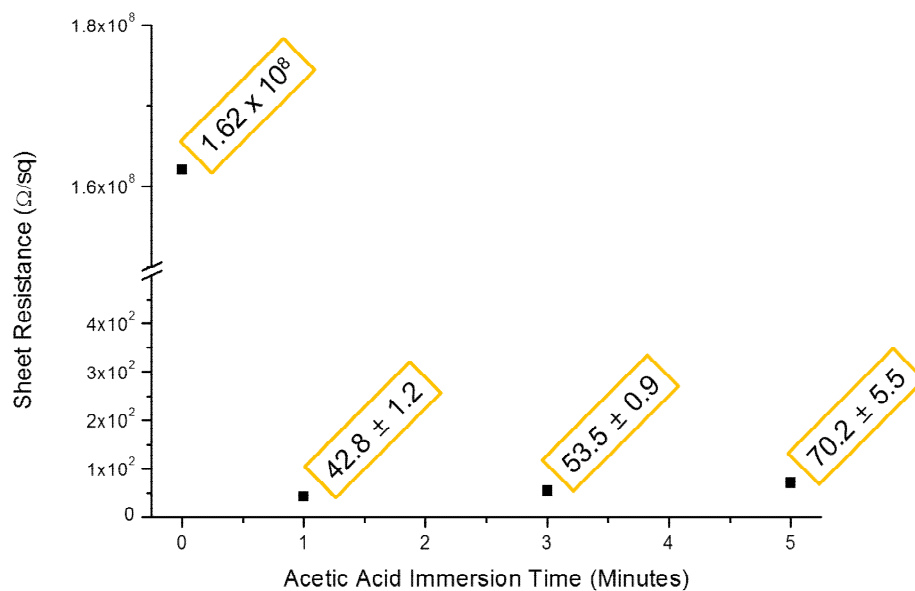


Figure 21. The sheet resistance changes of as-prepared Cu NP thin film with acetic acid immersion time. The sheet resistance dramatically decreased within 1 minute. However, after 3 minutes, the sheet resistance slightly increases due to excessive destruction of the surface of Cu NP films.

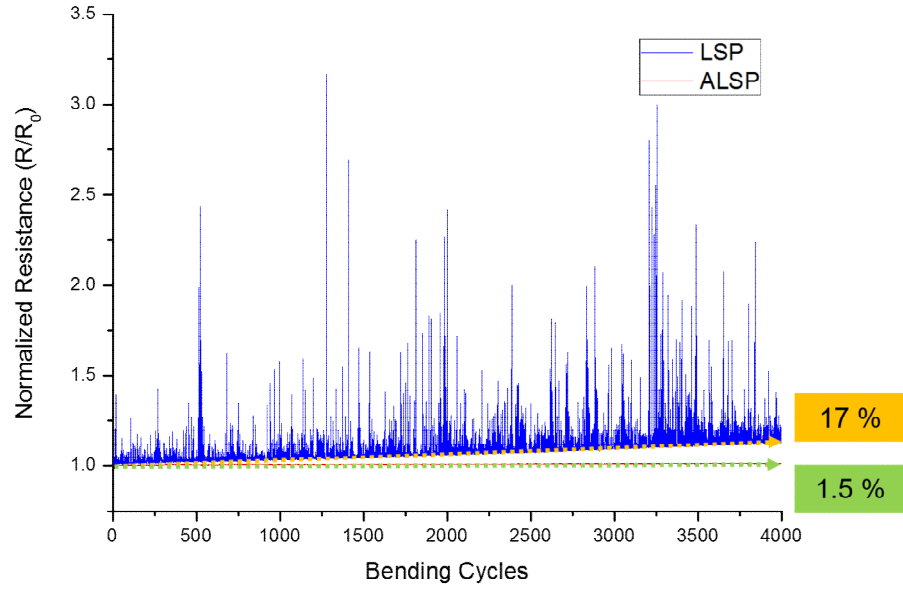


Figure 22. Cyclic bending test results for LSP and ASLP treated samples. In detail, the increasing rate of sheet resistance for ALSP treated Cu electrode is only 1.5 % with 4,000–cycle bending. On the other hand, the LSP showed over 17 % increasing rate of the sheet resistance with noise signals, which represent the unstable mechanical performance.

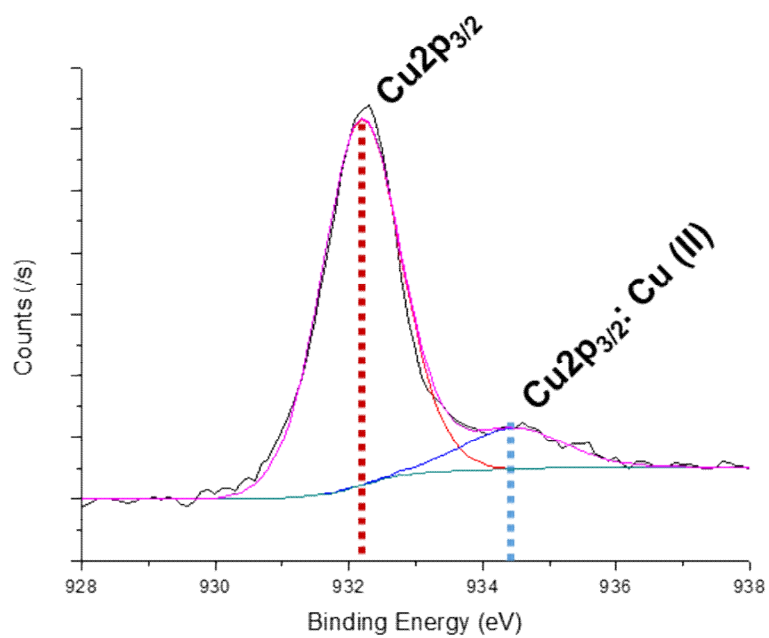


Figure 23. The XPS analysis for as-prepared Cu NP. The Cu NPs are slightly oxidized, which arise from the nanoparticle synthesis procedure.

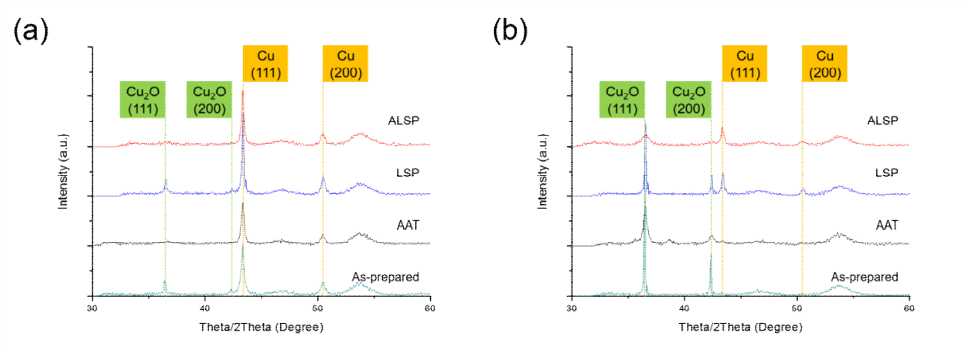


Figure 24. The XRD characterization of as-prepared, AAT, ASP and ALSP treated Cu NPs (a) before and (b) after high humidity-temperature test. The AAT process eliminates Cu oxides while as-fabricated Cu NPs are slightly oxidized. After humidity-temperature test, overall Cu NP samples are oxidized, which observed in Cu_2O (111, 200) peaks. Nevertheless, the ALSP treated Cu electrode is less oxidized than AAT and ASP treated ones.

Chapter 5 Experimental result : Mechano-thermo-chromic device with phase change and ALSP process

5.1. Operating mechanism

The basic working principle of the deliquescent salt-based mechano-thermo-chromic (MTC) device is represented in Figure 1 (a). The MTC device with the integrated transparent micro heater uses the sodium hydrate solution which shows unique three different phases with phase dependent optical properties (transparent for saturated/supersaturated sodium acetate solution, murky for sodium acetate trihydrate crystal) and phase change between them upon mechanical perturbation and heat. A simple chemical property such as a solubility of the salt in the water, i.e. water of crystallization, rules the nature of sodium acetate solution. Initially, an excessive amount of sodium acetate anhydrous (CH_3COONa) powder dissolved in deionized water at 65 oC until it reached transparent saturated solution state (stage 1). Afterward, the sodium acetate solution naturally cooled down to room temperature, subsequently; the solution became supersaturated while still transparent (stage 1 – 2). The state of the solution changed dramatically from transparent solution to opaque murky solid when the solution was subject to a mechanical stimulus (stage 2 – 3). The induced mechanical stimulus, i.e. an instant mechanical

impact on the sodium acetate solution with a sharp tip, caused supersaturated sodium acetate solution to form sodium acetate trihydrate crystal nucleus where the crystal growth started. The standard mechanical impact condition was studied by using spring-based impact measurement system (Figure S1(a) & S1(b), Table S2 & S3). The result signified that certain amount of mechanical impact energy (>40 mJ) is needed to initiate the crystallization of the sodium acetate. During the phase transition in Figure S1(c), the volume change was negligible without shrinkage or expansion. While sodium acetate has two similar compounds including sodium acetate anhydrous (CH_3COONa , T_m : 324°C) and sodium acetate trihydrate ($\text{CH}_3\text{COONa} \cdot 3\text{H}_2\text{O}$, T_m : 58°C), only a noticeable difference over the compounds is the melting point and solubility in water. Typically, the sodium acetate anhydrous easily forms hydrates when it dissolves in water, therefore, the identity of the observed crystal in our study is sodium acetate trihydrate under 58°C . Considering the standard enthalpy for the CH_3COONa ($\Delta_f H^\circ_{298} = -709.32$ kJ/mol) and $\text{CH}_3\text{COONa} \cdot 3\text{H}_2\text{O}$ ($\Delta_f H^\circ_{298} = -1604$ kJ/mol), the major contents at the stage 2 and stage 3 is $\text{CH}_3\text{COONa} \cdot 3\text{H}_2\text{O}$.⁽³⁵⁾ This transition is reversible and the murky sodium acetate trihydrate crystal in stage 3 could return to clear saturated sodium acetate solution in stage 1 upon heating. This solution also cools down to room temperature in supersaturated state by natural convection heat transfer to environment (stage 2). Figure 1(b) shows the microscopic SEM observation of the surface morphology of the precipitated sodium acetate trihydrate crystal.

The crystal has an irregular ingot form (Figure 1 (b)–i. and ii.) with stacked lamellar structure (yellow dotted box, Figure 1 (b)–iii.) as well as spread–out ring pattern from the initial mechanical stimulus point. Moreover, many cracks (red dotted box, Figure 1 (b)–iv.) on the surface of the sodium acetate crystal will possibly act as light scattering points to increase the optical property change.

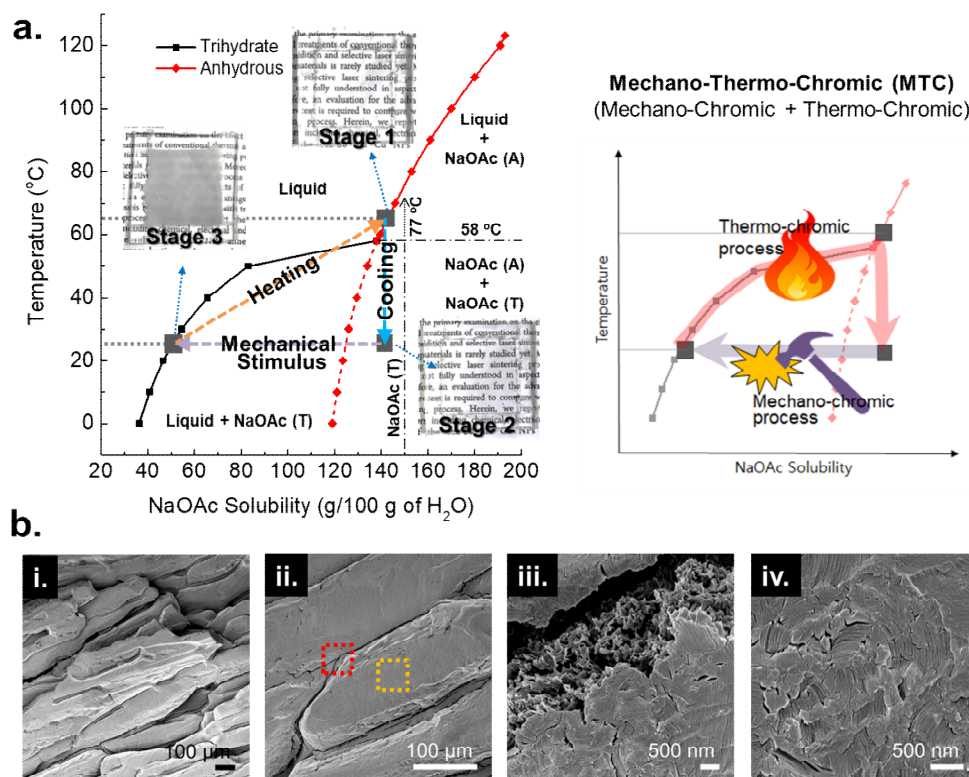


Figure 25. (a) Solubility graph at different temperature for sodium acetate anhydrous (CH_3COONa , red line) and sodium acetate trihydrate ($\text{CH}_3\text{COONa} \cdot 3\text{H}_2\text{O}$, black line) where the solid lines indicate saturated state. Insets show the digital pictures of MTC glass for various phase condition. Right graph shows the general process of mechano-thermo-chromic which is composed of mechano-chromic process and thermos-chromic process. (b) The microscopic surface morphology of sodium acetate crystal with i) low and ii) high magnification SEM image. The red-dot box exhibits the boundary of the crystal and the yellow-dot box shows the surface, which has an irregular vertically stacked structure.

5.2. Fabrication of MTC device

The fabrication process of the MTC device is shown in Figure 2(a). The MTC device consists of three parts: a chamber, sodium acetate solution and a transparent micro heater. Glass blocks from 1 to 3 mm thickness and polydimethylsiloxane (PDMS) solution were used to make various dimensional chambers. Highly transparent, saturated sodium acetate solution was prepared in the syringe and kept on a hot plate until injection to the PDMS chamber to prevent the unexpected crystallization. The acid-assisted laser sintering process of copper nanopaste offered a transparent micro heater on the flexible polyethylene terephthalate (PET) substrate. The fabricated micro heater on the flexible substrate had good electrical, chemical and mechanical stability, which examined in the previous study.⁽³⁶⁾ Afterward, the PDMS chamber and the transparent micro heater were bonded together for the salt solution sealing and for the stress accommodation during the formation of crystal nucleus. To find an optimum optical changeable transparency property for the MTC device, simple studies practiced on the various chamber dimensions without transparent heater (denoted as MTC glass). As shown in Figure 2(b), the chambers with liquid state of sodium acetate had clear appearances because the salt solution has high transparency; it rarely hindered overall transparency of the PDMS chamber. Accordingly, letters on a paper were visible through the MTC glass placed on the paper. The

optical property dependency on the salt crystal thickness was studied for MTC glass sample with various thickness (chamber 1,2,3 has thickness of 1,2,3 mm respectively). Although the transmittance of each chamber in liquid state of sodium acetate was very high, the transparency of MTC glass gradually decreased as thickness of the chamber increased after crystallization (Figure 2(c)). Moreover, Figure S2(a) shows the transmittance and haze factor variation with phase change, where the haze dramatically increased over 90% with a murky state for the all cases.

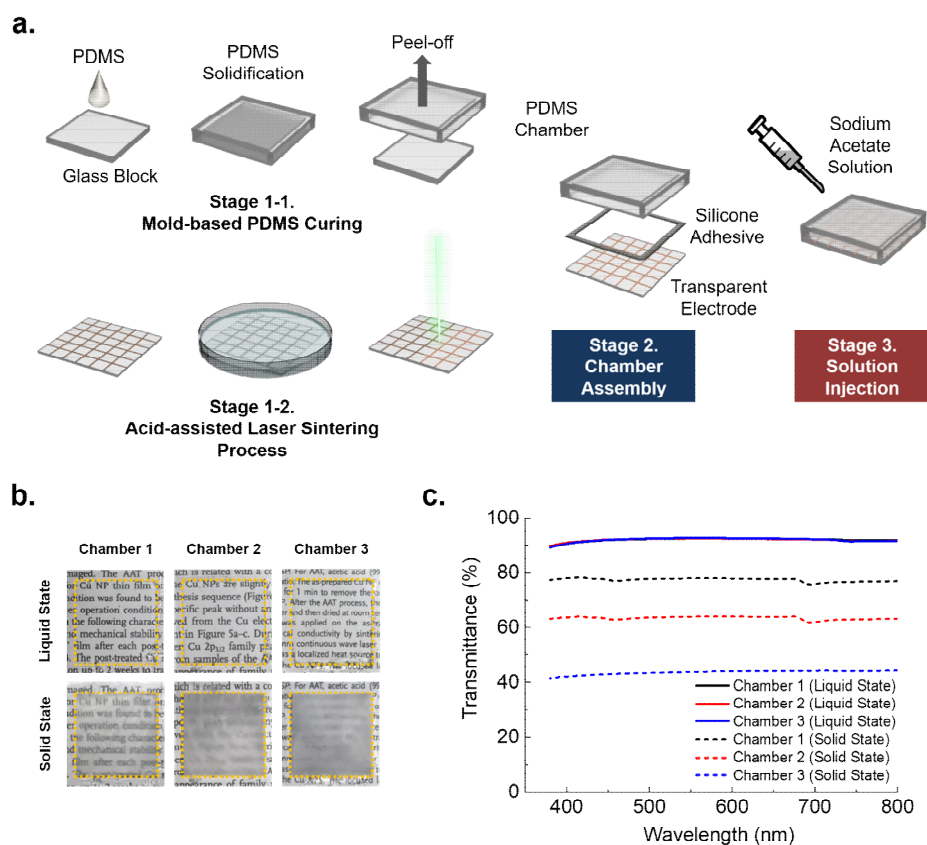


Figure 26. (a) The fabrication process of MTC device which consisted of a chamber for sodium acetate solution and the transparent micro heater processed prepared by acid-assisted laser sintering of Cu nanoparticle paste. (b) The digital images and (c) UV-Vis analysis of the transparency shift after phase change for each chamber thickness.

5.3. Design of MTC device

Each state (stage 1–2–3) was reversible by thermal control. The crystalized sodium acetate in the chamber can return to clear liquid state upon mild heating (stage 3 – 1). Since the heat capacity of the sodium acetate for the solid–liquid transition varied depending on the size of the chambers and corresponding material volume, the required time was also different for the same elevated temperature environment. In order to calculate the phase change rate difference for the crystalized sodium acetate in each chamber, the MTC glass sample was placed on a hot plate at 70 oC. Transient digital camera images took to check the optical property change rate for the crystalized sodium acetate during heating (Figure 3(a)). The top image was a reference painting image printed on a paper. Each MTC glass was directly located and overlaid on the reference image for comparison. The first column images show a reference and initial crystalized chamber images. The chamber 1 returned to transparent liquid state of the sodium acetate after 5 minutes heating due to smaller volume of the sodium acetate solution in a chamber. Although the chamber 1 has fast transition time from murky solid to transparent saturated liquid state, it has relatively lower opacity at the crystalized murky state than other thicker chambers and the background image was still partially visible. Therefore, it cannot provide a satisfactory contrast change. In the thicker case (chamber 2), it changes into liquid phase within 10

minutes. Unlike chamber 1, it provided sufficient opacity for the sunlight block and security purpose. For thicker case (chamber 3), while a light scattering property was better than that of other chambers, it needed much more thermal energy to initiate the phase transition of the crystalized salt–solution with a prolonged process time as much as 15 minutes. Considering that the MTC device consists of an integrated structure of a sodium acetate and a transparent micro heater, it is important to examine the heating performance of the integrated transparent micro heater. The electro–thermal performance and transparency of the laser–processed transparent micro heater were characterized in Figure S2(b) and S2(c). The required electrical energy gradually increased to 0.68 W, 1.12 W, 1.78 W, 2.27 W and 3.91 W for the all MTC devices (Figure 3(b)). While all of the transparent micro heater consumed the same electrical energy, different heating responses were observed depending on the chamber thickness. Since the heat capacity of chamber 1 was smaller than that of other chambers, it showed fast responses for heating and cooling. Although the electro–thermal performance of the chamber 2 was slightly lower than chamber 1, it had moderate response time and fair temperature generation property for the MTC device. On the other hand, the chamber 3 showed a slow response time as well as an excessive electrical energy demand for providing enough thermal energy. Compared with chamber 1 & 3, as the case of chamber 2 represented a satisfactory optical property for 60% transparent from the crystalized sodium acetate and an adequate electro–

thermal performance from the transparent micro heater as around 70 °C at 2.27 W condition within several minutes, the MTC device was fabricated with the condition of chamber 2.

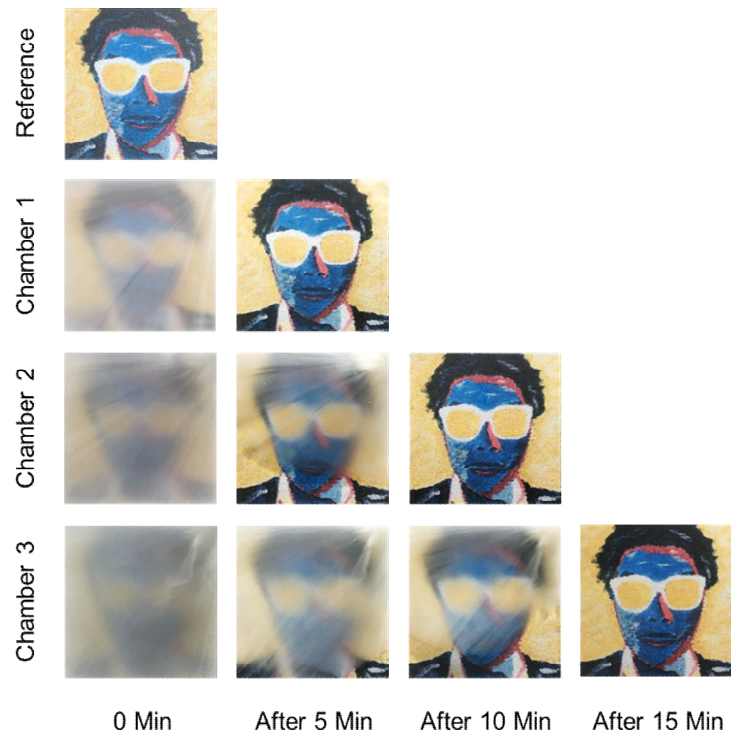
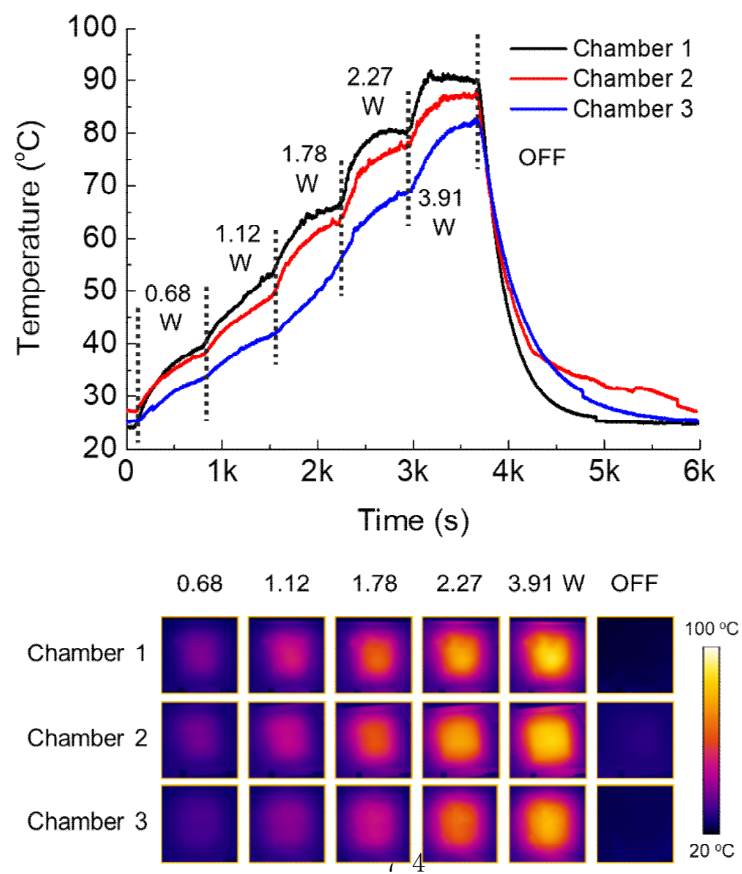
a.**b.**

Figure 27. (a) The optical characteristics change during the phase change of the sodium acetate crystal for each chamber at 70 oC heating. Background picture was used by courtesy of Jinhyeong Kwon. (b) The transient temperature measurement and corresponding IR camera images for the electro-thermal performance and temperature distribution of the transparent microheater depending on the thickness of each chamber.

5.4. Phase transition behavior of MTC device

The fabricated MTC device was characterized for various aspects including spectral transmittance, cyclic operation performance, transition speed and exothermic reaction. Since the sodium acetate changes from liquid to crystal reversibly by thermal control, transparency and haze factor of the MTC device varies from 80% for transparent liquid state to 40% for murky crystal state (Figure 4(a), Figure S2(d)). The transmittance sharply dropped near the 400 nm wavelength due to the UV-curable epoxy resin in the transparent micro heater strongly absorbed the UV wavelength (Figure S2(e)). The reversibility of the MTC device was confirmed by cyclic operation test (Figure 4(b)), where more experiments were conducted up to 200 cycles in Figure S3(a). A real time transient transmission system with a photodetector measured the transition speed from crystal to liquid. (Figure S3(b)) The sodium acetate shifts from crystal to intermediate phase and liquid state by an external mechanical stimulation and an electro-thermal heat from the transparent micro heater. The MTC device showed good reliability and durability for the practical use. As shown in Figure 4(c), an optical visibility of the MTC device increased during the phase transition of sodium acetate from crystal to saturated liquid by the integrated transparent micro heater within 400 seconds. The transparent micro heater induced the phase change of the sodium acetate in 800 seconds. Since the difference

of solubility at 40 °C and 25 °C was only 14 g per 100 g of water, the precipitation amount variation for the MTC device was negligible. Therefore, the MTC device could operate again by mechanical stimulation within a few minutes. Meanwhile, the crystallization of sodium acetate was exothermic reaction and it released heat during the process. For this reason, experimental and theoretical investigations conducted to show the effect of the released exothermic heat during the phase transition for the MTC device and surrounding environment as shown in Figure 4(d). The measured temperature elevation trend followed the calculated temperature.⁽³⁷⁾ The elevated temperature saturated around 40 °C in this case and the sodium acetate crystal did not dissolve by an exothermal energy due to its solubility with water. The overall exothermic reaction occurred for 20 minutes (Supplementary Figure S2(f)) and the phase transition to liquid was even possible during the exothermic reaction by heating at 65 °C. A relationship between temperature and transmittance of the MTC device was presented in Figure 4(e). By controlling the phase state of sodium acetate, the MTC device showed a broad optical switchable range. Figure 4(f) shows the transient phase change of sodium acetate from liquid to solid and the temperature rise due to exothermal heat release. Photocurrent variations and corresponding digital photo images confirmed that the crystal growth speed was approximately 6.56 mm/s. As shown in Figure S4, the MTC device also shows good mechanical stability against the unexpected external stimulus without direct internal mechanical impact to the sodium acetate

solution. Although the impact energy (708.05 mJ) which could break the glass chamber applied to the MTC device more than 20 times, the sodium acetate solution at the device stayed in the liquid phase.

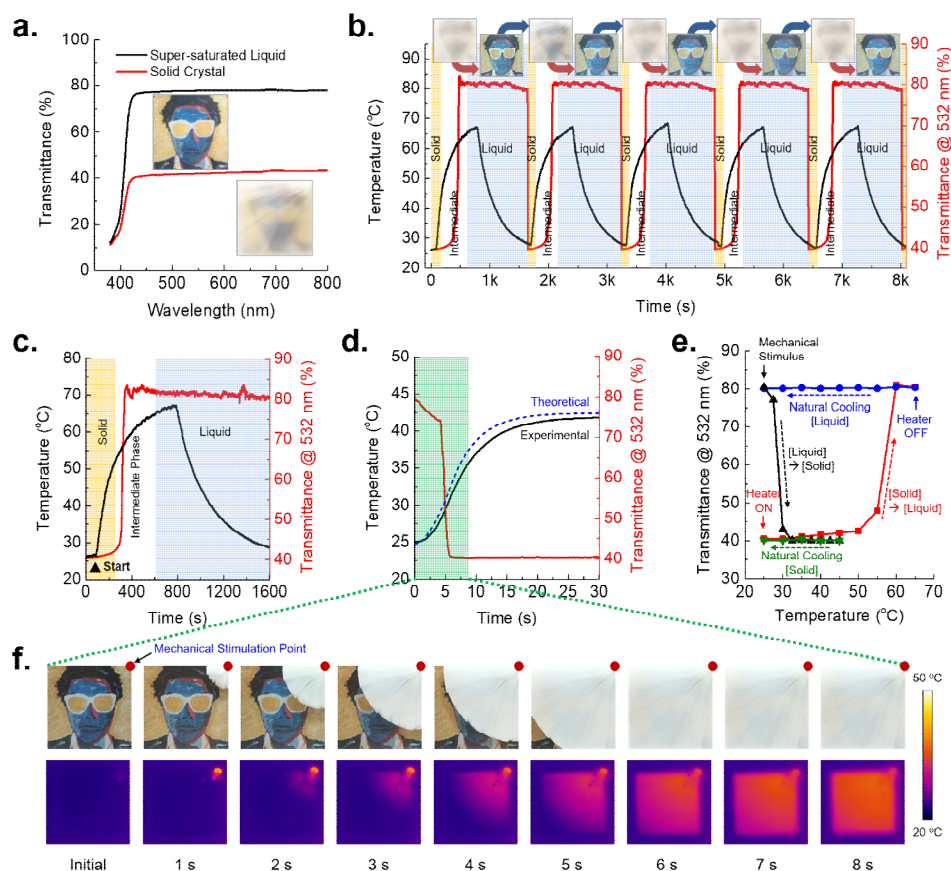


Figure 28. (a) Spectral transmittance of MTC devices integrated with the 2 mm thickness chamber (chamber 2) and the transparent micro heater represents for supersaturated liquid phase (black line) and crystallized solid phase (red line). (b) Cyclic operation test for the durability and reliability of the MTC device. Temperature (black line) and transmittance (red line) change were recorded along with the corresponding digital images. (c) Real-time variation of the temperature and transmittance during the transparent micro heater operation for phase change to liquid. (d) Real time measurement and calculation of temperature and transmission change during the exothermic phase change of sodium acetate crystallization. (e) A relationship between temperature and

transmittance of the MTC device during the one cycle operation. (i.) A sharp decline (black line) of transmittance by mechanical stimulus along with exothermic reaction. (ii.) Natural cooling (green line) after exothermal reaction with remaining low-transparency. (iii.) Phase transition to liquid (red line) by electothermal heat from a micro heater. (iv.) Natural cooling (blue line) after heating with remaining liquid state and high transmittance. (f) Digital picture and IR camera image during the sodium acetate crystal growth after mechanical stimulation impact at the right top corner of the sample (red dot).

5.5. Application of MTC device for smart glass

As a proof of concept for the practical application of MTC device in smart windows for a smart building system, a small MTC window and integrated control units reacting to the external environments enabled a simple miniaturized demonstration (Figure 5). The mockup system consists of a model house, 356 nm UV lamp to simulate a strong sunlight, MTC glass window, UV sensor, logic circuit, and other modules. The MTC device was established on the roof of the mockup model house and the painting image was placed behind the MTC device to show the optical property change. A window of the house held a UV sensor. Supplementary Figure S5 exhibited a logic flow chart for the MTC system operation. A mechanical stimulation module operated by a step motor generated a direct mechanical impact to the MTC system to initiate the phase transition of the sodium acetate from liquid to solid state. As shown in Figure 5(c), an UV irradiation as a trigger launched an operation of the MTC system. When the UV sensor detected the UV light irradiation, subsequently, stepping motor started to work to initiate the sodium acetate crystallization. Supplementary Video clip 1 shows the real time operation of MTC device. The MTC device changed to opaque state within few seconds. Afterward, when the intensity of UV light dropped below a critical level, the micro heater turned on to heat the MTC device and change the murky sodium acetate trihydrate crystal to transparent liquid state. The moment of

sodium acetate phase change in MTC device was recorded in Supplementary Video Clip 2. The MTC system can be easily scaled up for large area for smart window application. Different from the conventional electro-chromic system which needs prompt electrical energy to set the specific optical status, the optical property of MTC system could be changed by a simple mechanical perturbation and the optical status can be maintained without external energy input. The proposed MTC device may provide a novel and simple way for energy efficient next generation smart window.

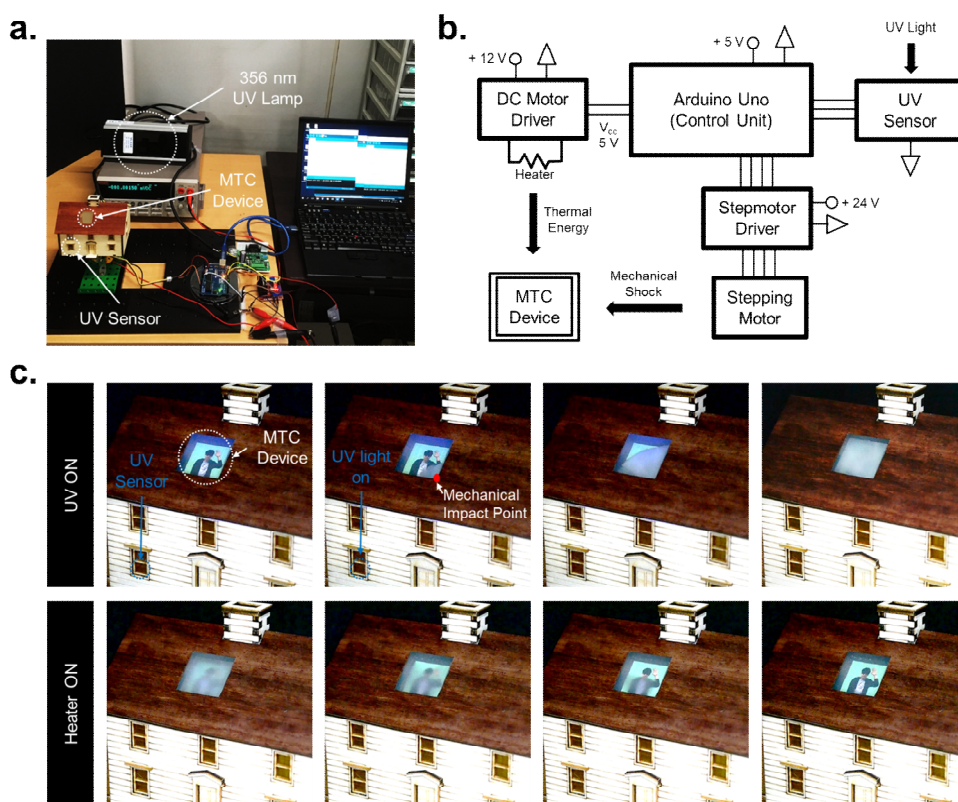


Figure 29. (a) A miniaturized mock-up demonstration with small MTC device-installed window and control units and (b) corresponding diagram. (c) Real time digital images during the operation of the MTC system. The irradiation of UV light works as trigger for the sodium acetate crystallization and corresponding optical property change. The transparent micro heater was turned on for phase transition from solid to liquid. Also see Supplementary Video Clips.

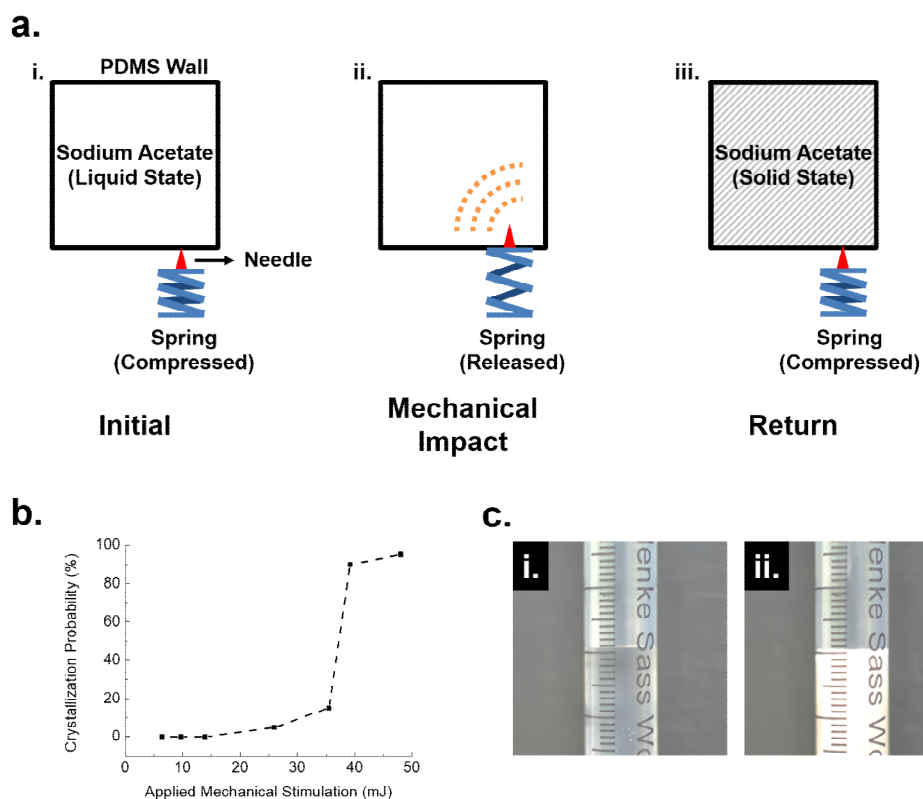


Figure 30. (a) Schematic model for a movement of syringe tip. Note that stored energy in the spring makes large mechanical impact instantly. A movement of the syringe tip was confined between 1st and 2nd hanger. (b) Crystallization probability was gradually increased in accordance to increase in applied mechanical power intensity. The standard mechanical stimulus was around 40 mJ. (c) Minor volume change was observed (i.) before and (ii.) after sodium acetate crystallization.

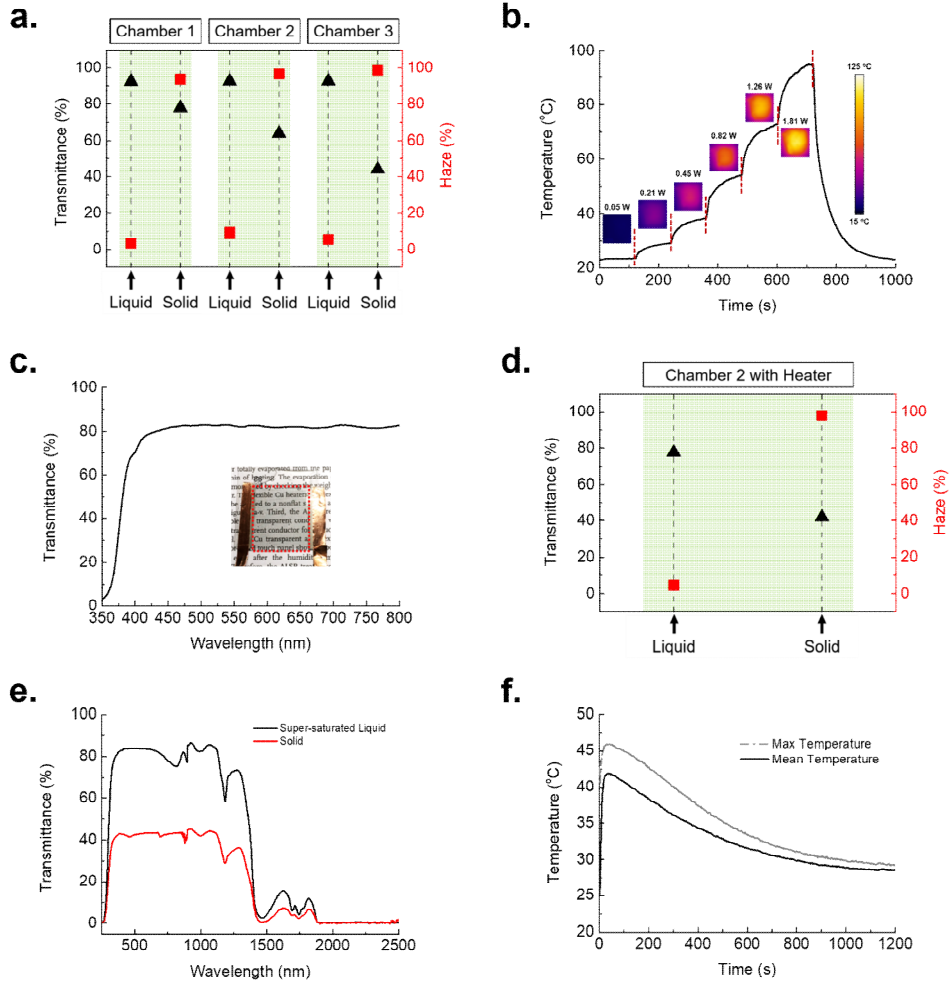


Figure 31. (a) The transmittance and haze variation with the sodium acetate phase change as liquid and solid for each chamber. (b) The heating performance characterization of the transparent micro heater fabricated by acid-assisted laser sintering process. (c) UV-Vis analysis of the micro heater processed by laser and UV-curable epoxy resin. (d) The transmittance and haze variation with the sodium acetate phase change for MTC device integrated with the 2 mm thickness chamber and the transparent micro heater. (e) The optical transmittance of the MTC device from wavelength of

250 - 2,500 nm. The crystalized (solid) state sodium acetate in MTC device can effectively block UV and visible light as well as IR wavelength region. (f) The overall temperature evolution during the crystallization of sodium acetate by the exothermal reaction.

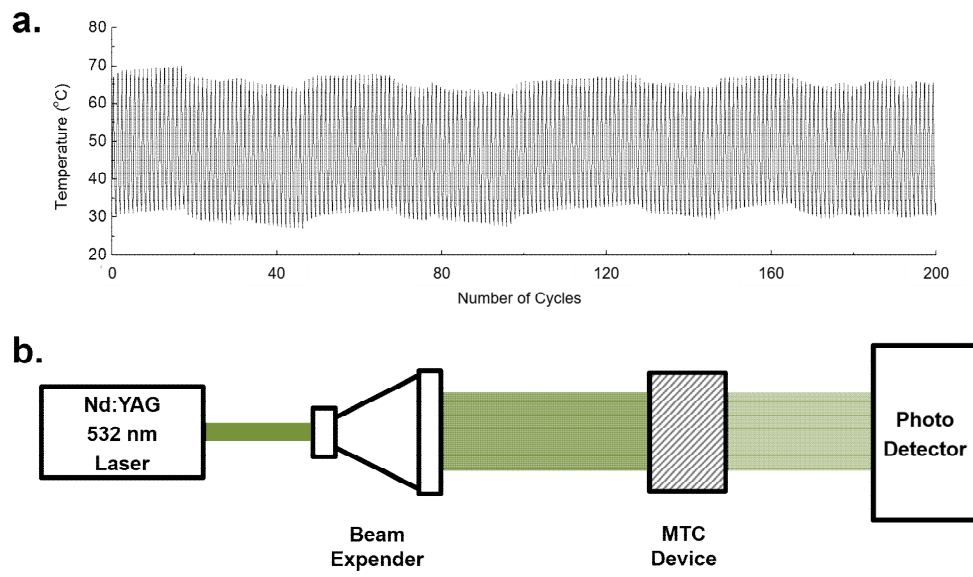


Figure 32. (a) The cyclic test up to 200 cycles shows the durability of MTC device without significant degradation. (b) The lab-made optical setup for verifying the transmitted light intensity variation with the phase of MTC device.

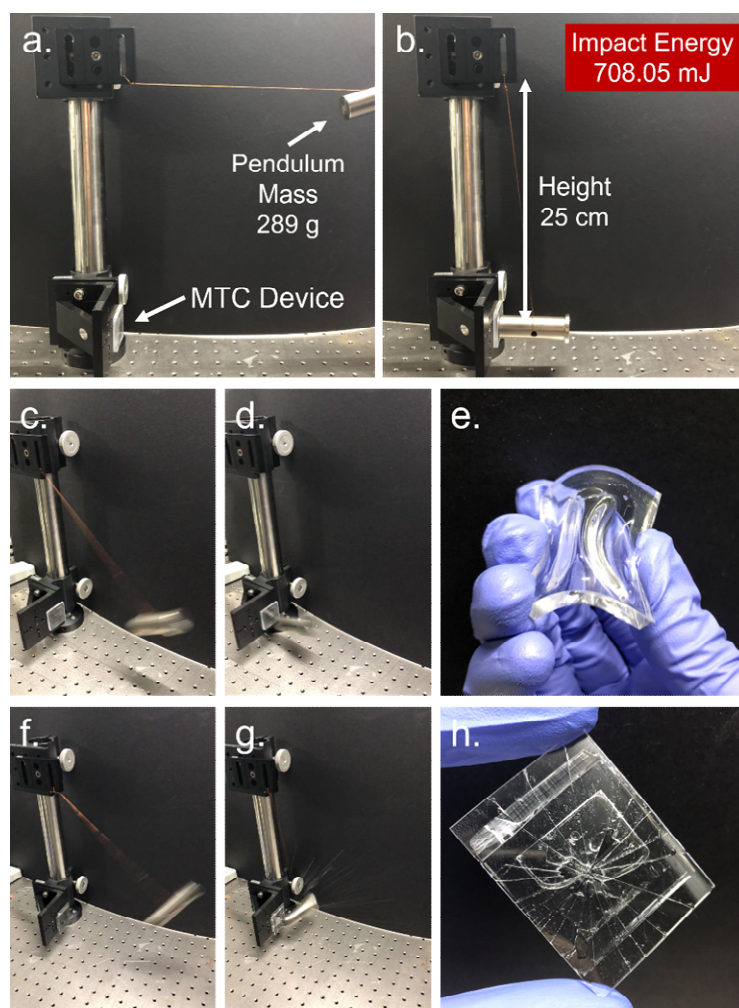


Figure 33. A pendulum impact test. The test conditions were represented in a–b. The calculated mechanical impact energy of the pendulum was approximately 708.05 mJ. A sodium acetate solution containing PDMS chamber, the MTC device, showed flawless appearance during and after the test in c–d. The MTC device was stable within external (unexpected) impact and even it beards high flexible state in e. A sodium acetate solution containing glass (surface) chamber was damaged after the same pendulum test in f–g. While the glass was broken by external impact, the sodium acetate solution stayed in solution state shown in h.

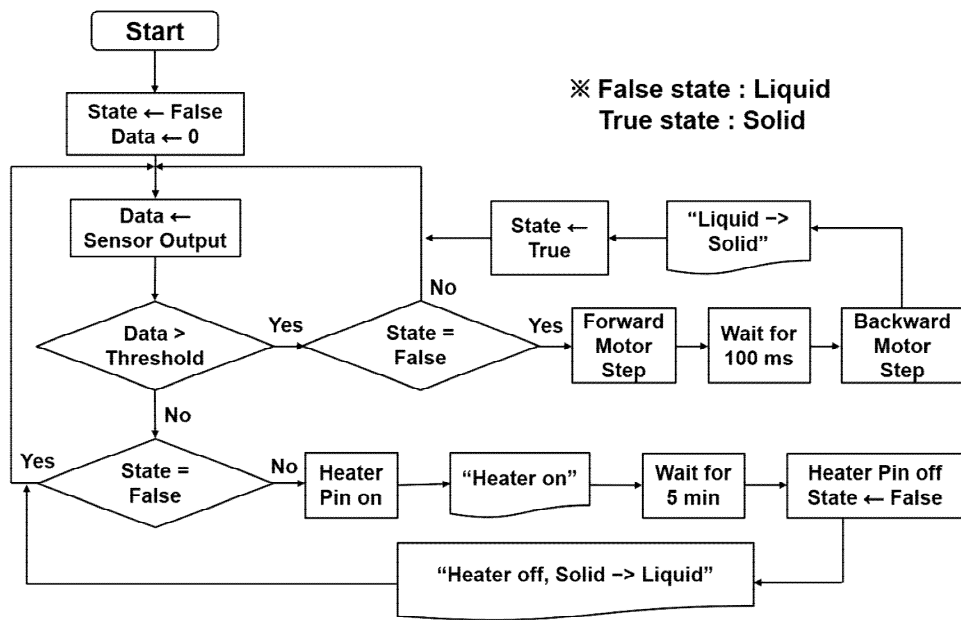


Figure 34. The logic flow chart for smart glass system integrated with MTC device and control units.

Chapter 6 Summary and future work

The Cu NPs are annealed by a conventional tube furnace heating and a selective laser sintering. The annealed Cu thin films are examined through various analytic tools. At first, Cu NPs are synthesized by polyol process and dispersed in liquid to make nanoparticle paste. TG-DTA measurement is practiced to verify the thermal activity of the Cu NP paste up to 500 °C. The Cu NP thin film are processed either by using conventional tube furnace heating in Ar environment or selective laser sintering in air environment. The laser-sintered Cu NP thin film exhibits superior electrical property, reduced oxidation and moderate chemical stability than general tube furnace heating process in sheet resistance measurement, XRD and XPS analysis. Consequently, the laser sintering process provides a rapid processing with a pronounced oxidation inhibition as well as improved chemical, electrical property than conventional thermal annealing process. Finally, the selective laser sintering process with the Cu NP paste can be implemented onto plastic substrate for flexible electronics applications with moderate electrical and mechanical stability.

Cu NP based flexible electrodes were prepared by various low temperature and low cost post-treatment methods including acetic acid treatment, laser sintering process and acid-assisted laser sintering process. The electrical conductivity of Cu electrode

was instantly enhanced by the AAT process. However, the surface morphology was changed into a rough surface with unstable property. While LSP treated Cu electrode shows good electrical conductivity, its mechanical stability including adhesion to the substrate showed unstable performance for the practice applications. To overcome the disadvantages of AAT and LSP treatment, ALSP was developed in this study. The ALSP treated Cu NP film showed superior chemical, electrical and mechanical property as well as more energy efficient process with an oxidation suppression in room temperature compared with other post-treatments. Finally, as a proof of concept, ALSP treated Cu electrodes were applied to fabricate flexible applications such as flexible and transparent heater and touch screen panel.

I developed a new method for the active optical property control for the next generation smart window application. While conventional electro-chromic devices apply electric field to electro-chromic or liquid crystal material for optical property control, this study represents a new concept transparency smart window using totally new driving mechanism (mechanical stimulus and thermal energy) to control the optical properties of the salt hydrate. This developed mechano-thermo-chromic (MTC) device with the integrated transparent micro heater uses the sodium hydrate solution which shows a unique dramatic optical property change under mechanical perturbation and heat. As a proof-of-concept for the practical application of MTC device in smart windows for a smart building system, a small MTC window and

integrated control units reacting to the external environments made possible a simple miniaturized demonstration. The MTC device can be easily scaled up for mass production and applied for flexible substrate for non-planar surface mounting. While the phase transition from the transparent supersaturated liquid to murky crystal is fast, the slow reverse phase transition from solid phase to liquid phase of the sodium acetate may be improved by adjusting solubility of sodium acetate in water and by maximizing heat generation via further optimized micro heater design. The developed mechano-thermo-chromic devices are expected to provide a useful approach in the future smart window applications which operates by an external environment condition such as intense UV light or deliberate mechanical impact from a user.

References

- (1) Roduner, E. Size Matters: Why Nanomaterials Are Different. *Chem. Soc. Rev.* 2006, 35, 583–592.
- (2) Cargnello, M.; Doan–Nguyen, V. V. T.; Gordon, T. R.; Diaz, R. E.; Stach, E. A.; Gorte, R. J.; Fornasiero, P.; Murray, C. B. Control of Metal Nanocrystal Size Reveals Metal–support Interface Role for Ceria Catalysts. *Science* 2013, 341, 771–773.
- (3) Leonard, F.; Talin, A. A. Electrical Contacts to One– and Two–dimensional Nanomaterials. *Nat. Nanotechnol.* 2011, 6, 773–783.
- (4) Rahul, S. H.; Balasubramanian, K.; Venkatesh, S. Inkjet Printing of Yttria Stabilized Zirconia Nano Particles on Metal Substrates. *Int. J. Precis. Eng. Man.* 2015, 16, 2553–2561.
- (5) Lee, J.; Lee, P.; Lee, H.; Lee, D.; Lee, S. S.; Ko, S. H. Very Long Ag Nanowire Synthesis and Its Application in a Highly Transparent, Conductive and Flexible Metal Electrode Touch Panel. *Nanoscale* 2012, 4, 6408–6414.
- (6) Hong, S.; Yeo, J.; Kim, G.; Kim, D.; Lee, H.; Kwon, J.; Lee, H.; Lee, P.; Ko, S. H. Nonvacuum, Maskless Fabrication of a Flexible Metal Grid Transparent Conductor by Low–temperature Selective Laser Sintering of Nanoparticle Ink. *ACS Nano* 2013, 7, 5024–5031.
- (7) Thiemann, S.; Gruber, M.; Lokteva, I.; Hirschmann, J.; Halik, M.; Zaumseil, J. High–Mobility ZnO Nanorod Field–effect Transistors by Self–Alignment and Electrolyte–Gating. *ACS App. Mater. Interfaces* 2013, 5, 1656–1662.
- (8) Kim, Y.–H.; Heo, J.–S.; Kim, T.–H.; Park, S.; Yoon, M.–H.; Kim, J.; Oh, M. S.; Yi, G.–R.; Noh, Y.–Y.; Park, S. K. Flexible Metal–oxide Devices Made by Room–temperature Photochemical Activation of Sol–gel Films. *Nature* 2012, 489, 128–132.
- (9) Pu, J.; Yomogida, Y.; Liu, K.–K.; Li, L.–J.; Iwasa, Y.; Takenobu, T. Highly Flexible MoS₂ Thin–film Transistors with Ion Gel Dielectrics. *Nano Lett.* 2012, 12, 4013–4017.
- (10) Aziz, H.; Popovic, Z. D.; Hu, N.–X.; Hor, A.–M.; Xu, G. Degradation Mechanism of Small Molecule–based Organic Light–emitting Devices. *Science* 1999, 283, 1900–1902.

- (11) Tao, Y.; Wang, Q.; Yang, C.; Zhong, C.; Qin, J.; Ma, D. Multifunctional Triphenylamine/Oxadiazole Hybrid as Host and Exciton-blocking Material: High Efficiency Green Phosphorescent OLEDs Using Easily Available and Common Materials. *Adv. Funct. Mater.* 2010, 20, 2923–2929.
- (12) Hong, S.; Lee, H.; Lee, J.; Kwon, J.; Han, S.; Suh, Y. D.; Cho, H.; Shin, J.; Yeo, J.; Ko, S. H. Highly Stretchable and Transparent Metal Nanowire Heater for Wearable Electronics Applications. *Adv. Mater.* 2015, 27, 4744–4751.
- (13) Ko, S. H. A Review of the Multi-scale Nano-structure Approach to the Development of High Efficiency Solar Cells. *Smart Science* 2014, 2, 54–62.
- (14) Kwon, J.; Hong, S.; Lee, H.; Yeo, J.; Lee, S.; Ko, S. Direct Selective Growth of ZnO Nanowire Arrays from Inkjet-printed Zinc Acetate Precursor on a Heated Substrate. *Nanoscale Res. Lett.* 2013, 8, 1–6.
- (15) Pan, L.; Chortos, A.; Yu, G.; Wang, Y.; Isaacson, S.; Allen, R.; Shi, Y.; Dauskardt, R.; Bao, Z. An Ultra-Sensitive Resistive Pressure Sensor Based on Hollow-sphere Microstructure Induced Elasticity in Conducting Polymer Film. *Nat. Commun.* 2014, 5, 3002.
- (16) Lee, B. Y.; Sung, M. G.; Lee, J.; Baik, K. Y.; Kwon, Y.-K.; Lee, M.-S.; Hong, S. Universal Parameters for Carbon Nanotube Network-based Sensors: Can Nanotube Sensors Be Reproducible? *ACS Nano* 2011, 5, 4373–4379.
- (17) Choi, E. K.; Park, J.; Kim, B. S.; Lee, D. Fabrication of Electrodes and Near-field Communication Tags Based on Screen Printing of Silver Seed Patterns and Copper Electroless Plating. *Int. J. Precis. Eng. Man.* 2015, 16, 2199–2204.
- (18) Lu, L.; Shen, Y.; Chen, X.; Qian, L.; Lu, K. Ultrahigh Strength and High Electrical Conductivity in Copper. *Science* 2004, 304, 422–426.
- (19) Nath, P.; Chopra, K. L. Thermal Conductivity of Copper Films. *Thin Solid Films* 1974, 20, 53–62.
- (20) Athanassiou, E. K.; Grass, R. N.; Stark, W. J. Large-scale Production of Carbon-coated Copper Nanoparticles for Sensor Applications. *Nanotechnol.* 2006, 17, 1668–1673.
- (21) Yabuki, A.; Arriffin, N. Electrical Conductivity of Copper Nanoparticle Thin Films Annealed at Low Temperature. *Thin Solid Films* 2010, 518, 7033–7037.

- (22) Kwon, J.; Park, S.; Haque, M. M.; Kim, Y.-S.; Lee, C. S. Study of Sintering Behavior of Vapor Forms of 1-octanethiol Coated Copper Nanoparticles for Application to Ink-jet Printing Technology. *J. Nanosci. Nanotechnol.* 2012, 12, 3434–3437.
- (23) Norman, A. L.; Evagelos, K. A.; Wendelin, J. S. Graphene-stabilized Copper Nanoparticles as an Air-stable Substitute for Silver and Gold in Low-cost Ink-jet Printable Electronics. *Nanotechnol.* 2008, 19, 445201–445206.
- (24) Lee, Y.; Choi, J.; Lee, K. J.; Scott, N. E.; Kim, D. Large-scale Synthesis of Copper Nanoparticles by Chemically Controlled Reduction for Applications of Inkjet-Printed Electronics. *Nanotechnol.* 2008, 19, 415604–415610.
- (25) Anyaogu, K. C.; Fedorov, A. V.; Neckers, D. C. Synthesis, Characterization, and Antifouling Potential of Functionalized Copper Nanoparticles. *Langmuir* 2008, 24, 4340–4346.
- (26) Ryu, J.; Kim, H.-S.; Hahn, H. T. Reactive Sintering of Copper Nanoparticles Using Intense Pulsed Light for Printed Electronics. *J. Elec. Materi.* 2011, 40, 42–50.
- (27) Michael, Z.; Oleg, E.; Amir, S.; Zvi, K. Laser Sintering of Copper Nanoparticles. *J. Phys. D Appl. Phys.* 2014, 47, 025501–025511.
- (28) Han, S.; Hong, S.; Ham, J.; Yeo, J.; Lee, J.; Kang, B.; Lee, P.; Kwon, J.; Lee, S. S.; Yang, M.-Y.; Ko, S. H. Fast Plasmonic Laser Nanowelding for a Cu-nanowire Percolation Network for Flexible Transparent Conductors and Stretchable Electronics. *Adv. Mater.* 2014, 26, 5808–5814.
- (29) Watanabe, A.; Miuhita, T. Formation of Copper Micro-wiring by Laser Direct Writing. *J. Photopolym. Sci. Technol.* 2007, 20, 115–116.
- (30) Chio, T. Y.; Poulikakos, D.; Grigoropoulos, C. P. Fountain-pen-based Laser Microstructuring with Gold Nanoparticle Inks. *Appl. Phys. Lett.* 2004, 85, 13–15.
- (31) Watanabe, A.; Kobayashi, Y.; Konno, M.; Yamada, S.; Miwa, T. Direct Drawing of Ag Microwiring by Laser-induced Pyrolysis of Film Prepared from Liquid-dispersed Metal Nanoparticles, *Jpn. J. Appl. Phys.* 2005, 44, 20–23.
- (32) Aminuzzaman, M.; Watanabe, A.; Miyashita, T. Direct Writing of Conductive Silver Micropatterns on Flexible Polyimide Film by Laser-induced Pyrolysis of Silver Nanoparticle-dispersed Film. *J. Nanopart. Res.* 2010, 12, 931–938.

- (33) Aminuzzaman, M.; Watanabe, A.; Miyashita, T. Photochemical Surface Modification and Characterization of Double-decker-shaped Polysilsesquioxane Hybrid Thin Films. *J. Mater. Chem.* 2008, 18, 5092–5097.
- (34) Liu, Y.; Sie, Y.; Liu, C.; Lee, M.-T. A Novel Laser Direct Writing System Integrated with A&F XXY Alignment Platform for Rapid Fabrication of Flexible Electronics. *Smart Science* 2015, 3, 87–91.
- (35) Chu, W.; Kim, C.; Lee, H.; Choi, J.; Park, J.; Song, J.; Jang, K.; Ahn, S.-H. Hybrid Manufacturing in Micro/Nano Scale: A Review. *Int. J. Precis. Eng. Man.-Green Tech.* 2014, 1, 75–92.
- (36) Paeng, D.; Lee, D.; Yeo, J.; Yoo, J.-H.; Allen, F. I.; Kim, E.; So, H.; Park, H. K.; Minor, A. M.; Grigoropoulos, C. P. Laser-induced Reductive Sintering of Nickel Oxide Nanoparticles under Ambient Conditions. *J. Phys. Chem. C* 2015, 119, 6363–6372.
- (37) Necmi, S.; Tülay, S.; Şeyda, H.; Yasemin, Ç. Annealing Effects on the Properties of Copper Oxide Thin Films Prepared by Chemical Deposition. *Semi. Sci. Technol.* 2005, 20, 398–401.
- (38) Poulston, S.; Parlett, P. M.; Stone, P.; Bowker, M. Surface Oxidation and Reduction of CuO and Cu₂O Studied Using XPS and XAES. *Surf. Interface Anal.* 1996, 24, 811–820.
- (39) Pollock, N.; Fowler, G.; Twyman, L. J.; McArthur, S. L. Synthesis and Characterization of Immobilized PAMAM Dendrons. *Chem. Commun.* 2007, 2482–2484.
- (40) Hoppe, C. E.; Lazzari, M.; Pardiñas-Blanco, I.; López-Quintela, M. A. One-Step Synthesis of Gold and Silver Hydrosols Using Poly(N-vinyl-2-pyrrolidone) as a Reducing Agent. *Langmuir* 2006, 22, 7027–7034.
- (41) Washio, I.; Xiong, Y.; Yin, Y.; Xia, Y. Reduction by the End Groups of Poly(vinyl pyrrolidone): A New and Versatile Route to the Kinetically Controlled Synthesis of Ag Triangular Nanoplates. *Adv Mater.* 2006, 18, 1745–1749.
- (42) R. Kas, K. K. Hummadi, R. Kortlever, P. de Wit, A. Milbrat, M. W. J. Luiten-Olieman, N. E. Benes, M. T. M. Koper, G. Mul, *Nat Commun* 2016, 7.
- (43) Y. Lee, T.-S. Kim, S.-Y. Min, W. Xu, S.-H. Jeong, H.-K. Seo, T.-W. Lee,

- Advanced Materials 2014, 26, 8010.
- (44) E. M. Hicks, X. Zhang, S. Zou, O. Lyandres, K. G. Spears, G. C. Schatz, R. P. Van Duyne, The Journal of Physical Chemistry B 2005, 109, 22351.
- (45) J. Song, J. Li, J. Xu, H. Zeng, Nano Letters 2014, 14, 6298.
- (46) Y. Tang, S. Gong, Y. Chen, L. W. Yap, W. Cheng, ACS Nano 2014, 8, 5707.
- (47) E. Roduner, Chemical Society Reviews 2006, 35, 583.
- (48) L. Xu, Y. Yang, Z.-W. Hu, S.-H. Yu, ACS Nano 2016, 10, 3823.
- (49) E. K. Athanassiou, R. N. Grass, W. J. Stark, Nanotechnology 2006, 17, 1668.
- (50) K. C. Anyaogu, A. V. Fedorov, D. C. Neckers, Langmuir 2008, 24, 4340.
- (51) L. Youngil, C. Jun-rak, L. Kwi Jong, E. S. Nathan, K. Donghoon, Nanotechnology 2008, 19, 415604.
- (52) H.-C. Chu, Y.-C. Chang, Y. Lin, S.-H. Chang, W.-C. Chang, G.-A. Li, H.-Y. Tuan, ACS Applied Materials & Interfaces 2016, 8, 13009.
- (53) S. An, H. S. Jo, D.-Y. Kim, H. J. Lee, B.-K. Ju, S. S. Al-Deyab, J.-H. Ahn, Y. Qin, M. T. Swihart, A. L. Yarin, S. S. Yoon, Advanced Materials 2016, n/a.
- (54) Z. Zhong, H. Lee, D. Kang, S. Kwon, Y.-M. Choi, I. Kim, K.-Y. Kim, Y. Lee, K. Woo, J. Moon, ACS Nano 2016.
- (55) J. H. Park, S. Jeong, E. J. Lee, S. S. Lee, J. Y. Seok, M. Yang, Y. Choi, B. Kang, Chemistry of Materials 2016, 28, 4151.
- (56) S. Han, S. Hong, J. Ham, J. Yeo, J. Lee, B. Kang, P. Lee, J. Kwon, S. S. Lee, M.-Y. Yang, S. H. Ko, Advanced Materials 2014, 26, 5808.
- (57) S. Bhanushali, P. Ghosh, A. Ganesh, W. Cheng, Small 2015, 11, 1232.
- (58) M. Jin, G. He, H. Zhang, J. Zeng, Z. Xie, Y. Xia, Angewandte Chemie International Edition 2011, 50, 10560.
- (59) Z. Yin, C. Lee, S. Cho, J. Yoo, Y. Piao, Y. S. Kim, Small 2014, 10, 5047.
- (60) M. Singh, H. M. Haverinen, P. Dhagat, G. E. Jabbour, Advanced Materials 2010, 22, 673.
- (61) T. Zhang, X. Wang, T. Li, Q. Guo, J. Yang, Journal of Materials Chemistry C 2014, 2, 286.
- (62) Y. Hokita, M. Kanzaki, T. Sugiyama, R. Arakawa, H. Kawasaki, ACS Applied Materials & Interfaces 2015, 7, 19382.

- (63) H. Kang, E. Sowade, R. R. Baumann, *ACS Applied Materials & Interfaces* 2014, 6, 1682.
- (64) J. Yeo, S. Hong, D. Lee, N. Hotz, M.-T. Lee, C. P. Grigoropoulos, S. H. Ko, *PLoS ONE* 2012, 7, e42315.
- (65) C. Mayousse, C. Celle, A. Carella, J.-P. Simonato, *Nano Research* 2014, 7, 315.
- (66) J. Kwon, H. Cho, H. Eom, H. Lee, Y. D. Suh, H. Moon, J. Shin, S. Hong, S. H. Ko, *ACS Applied Materials & Interfaces* 2016, 8, 11575.
- (67) Y. D. Suh, S. Hong, J. Lee, H. Lee, S. Jung, J. Kwon, H. Moon, P. Won, J. Shin, J. Yeo, S. H. Ko, *RSC Advances* 2016, 6, 57434.
- (68) G. G. Jernigan, G. A. Somorjai, *Journal of Catalysis* 1994, 147, 567.
- (69) T. Ghodselahi, M. A. Vesaghi, A. Shafiekhani, A. Baghizadeh, M. Lameii, *Applied Surface Science* 2008, 255, 2730.

Abstract

레이저-구리 나노입자 상호작용 공정을 활용하여 산화 억제된
투명하고 유연한 구리 전자소자 제작

구리는 낮은 가격 및 높은 전도도 특성 때문에 전극 소재로 각광받아 왔다. 하지만 대기중의 산소나 수증기와 반응하여 산화되기 쉽고, 실제 제작 가공이나 사용에 있어서 소재 특성이 바뀌는 단점이 있다. 기존에는 이러한 단점을 보완하기 위하여 고진공 또는 비활성기체환경에서의 열처리를 통하여 소자를 제작하는 공정을 활용해 왔다. 하지만 기존의 열처리 공정은 열에 취약한 플렉서블 기판위에 소자제작을 어렵게 한다. 그리고 전극 회로 패터닝을 위하여 기존의 금속 식각공정을 사용해 왔는데 패터닝을 노광하기 위한 마스크 제작, 유해 용액 사용, 복잡한 다수의 공정 도입 등으로 유지 및 제작비용이 급격하게 상승하게 된다. 따라서 본 연구에서는 구리 나노 입자를 활용한 산화 억제 및 직접 패터닝 제작을 위하여 구리 나노 물질 인쇄 및 코팅 공정/레이저 융합 공정 개발/소자 회로 설계 및 제작/실제 소자 특성 측정 및 평가에 관한 연구를 했다.

구리 나노 입자는 폴리올 공정을 통하여 합성하고 직접 인쇄 전자 및 용액 공정으로 활용하기 위하여 잉크화하여 사용하였다. 구리 나노 입자는 부피 대비 표면적의 비가 높아 기존의 구리 보다 더 빠르게 산화되기 쉽다. 그래서 구리 나노 입자의 산화를 방지하기 위하여 표면을 폴리머층으로 감싸 보호하였다. 또한 구리 나노 입자의 잉크화를 통하여 다양한 직접 패터닝 공정으로 활용이 용이하고, 이러한 직접

공정들을 활용하여 플렉시블/스트레처블 기판위에 소자 및 어레이를 제작하는 하는 방향으로 연구하였다. 나노 입자는 입자의 크기, 형상, 소재 종류에 따라 각각 다른 광학적 특성을 가지고 있다. 특히 구리 나노 입자는 특정 빛 파장 영역(600nm 부근)에서 흡광도가 높아 집광된 단파장의 레이저를 이용한 광-열 반응 공정에 적용하기 용이하다. 그리고 구리 나노 입자의 표면에 있는 보호층 폴리머와 고유한 구리 산화층이 광-열반응 과정에서 화학적 환원 반응이 유도되어 전도성이 향상되는 효과를 볼 수 있었다. 이러한 화학 반응과 더불어 레이저 직접 고속처리를 통하여 높은 온도에서의 유지시간을 줄여줘서 소자 제작 공정 시 산화를 방지할 수 있었다. 선택적 레이저 용접 공정은 국소 레이저 처리된 부분만 전극제작이 가능하여 직접 패턴이 가능하고 패턴에 사용되지 않은 구리 나노 입자 잉크는 재사용이 가능하다.

선택적 레이저 용접공정에 추가하여 산 용액 처리 공정을 접목하여 내산화성 및 기계적 안정성이 획기적으로 향상된 구리 전극을 제작하였다. 구리 나노 입자 표면의 산화구리 및 폴리머 보호층을 카르복실 계열의 산으로 처리하여 제거한 후 레이저 용접 처리를 하게 되면 전극 표면의 다공성이 획기적으로 줄어들게 된다. 구리 기반의 전극에서 다공성이 높을수록 대기의 산소 및 수증기와 반응하는 표면적이 늘어나 산화에 취약한 단점이 있지만 카르복실 계열의 산 처리를 도입함으로써 표면의 다공성을 낮출 수 있을 뿐만 아니라 용접된 구리 나노 입자 사이의 산화구리를 제거하는 효과도 있어 고 순도의 구리로 전극제작을 가능하게 한다. 산-보조 레이저 용접 공정은 기존의 레이저 공정의 장점과 더불어 제작되는 소자의 성능을 획기적으로 향상시킬 수 있다.

선택적 레이저 용접공정, 산-보조 레이저 용접공정을 활용하여 투명

유연/신축 터치 패널 어레이, 전-열 장치, 상변화 기반 스마트 윈도우 소자 제작으로 활용했다. 본 연구의 공정으로 제작한 투명 유연/신축 전극은 내산화성, 내구성, 투명성, 작동 안정성 등의 장점이 있어 실제 구리 전극 기반의 소자 전극 제작으로 공정 활용 가능성을 넓혀 갈 수 있을 것으로 기대된다.

주요어 : 산화 억제, 구리 나노 입자, 선택적 레이저 용접공정, 산-보조 레이저 용접공정, 투명 유연 전극 어레이

학 번 : 2014-21833